Icarus 415 (2024) 116076

Contents lists available at ScienceDirect

Icarus

journal homepage: www.elsevier.com/locate/icarus

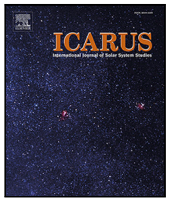

Research Paper

Atmospheric gravity waves in Venus dayside clouds from VIRTIS-M images

José E. Silva [a,*], Javier Peralta [b], Alejandro Cardesín-Moinelo [c,d,f], Ricardo Hueso [e], Daniela Espadinha [f], Yeon Joo Lee [a]

[a] Planetary Atmospheres Group, Institute for Basic Science, 55, Expo-ro, Yuseong-gu, Daejeon, 34126, Republic of Korea
[b] Departamento de Física Atómica, Molecular y Nuclear, Facultad de Física, Universidad de Sevilla, San Fernando, 4, Sevilla, Andalucía, Spain
[c] European Space Astronomy Centre, Camino Bajo del Castillo s/n, Villafranca del Castillo, Madrid, 28692, Spain
[d] Institute of Astrophysics of Andalucia, Glorieta de la Astronomía s/n, Granada, 18008, Spain
[e] Departamento de Física Aplicada, Escuela de Ingeniería de Bilbao, Universidad del País Vasco/Euskal Herriko Unibertsitate, Universidad del País Vasco/Euskal Herriko Unibertsitatea Barrio Sarriena s/n Leioa Bizkaia, Bilbau, 48940, Spain
[f] Institute of Astrophysics and Space Sciences, University of Lisbon, Astronomical Observatory of Lisbon, Tapada da Ajuda, East Building – 2nd floor, Lisbon, 1349-018, Portugal

ARTICLE INFO

Keywords:
Atmospheres
Dynamics
Ultraviolet observations
Venus
Atmosphere

ABSTRACT

We perform a survey of the Visible and Infrared Thermal Imaging Spectrometer-Mapper (VIRTIS-M) images onboard the Venus Express space mission, at four narrow wavelength bands that target different altitude regions on the cloud deck of Venus' atmosphere (280–320, 365–400, 580–600, 900–920 nm). Our goal was to detect and characterize atmospheric gravity waves, using several processing techniques based on high-pass filtering to enhance features in low-contrast images. The period of our selected dataset was between August 2007–October 2008 on the dayside hemisphere, identical to a previous study of waves located on the nightside lower cloud, so that a temporally overlapped comparison could be established, although over different longitudinal locations. We retrieved the morphological properties of these waves including horizontal wavelength and packet width along with several orientations of the identified waves. We retrieved properties for 69 wave packets across all analysed wavelength ranges, and dynamical parameters for 16 wave packets.

Waves observed across the four wavelength ranges examined here have similar properties, with horizontal wavelengths of a few hundred kilometres and full length of wave-trains going up to 1000 km. Although these wave properties do not seem to depend on latitude, we notice an increase in the values of several of these parameters close to the evening terminator. Considering our results and a comparison with previous studies of stationary features interpreted as gravity waves, we argue that forcing from topography is not the main cause of the wave packets observed here, whose properties are better supported by a convective generation scenario.

The retrieved properties show a consistent agreement between waves on the upper and lower cloud, suggesting a similar forcing mechanism based on convection from a neutral stability layer between the lower and middle-upper cloud. Despite the similar properties, we find no evidence of any correlation between wave packets propagating in the lower cloud and upper cloud, based on their shape and relative position.

1. Introduction

Gravity waves are a recurring phenomenon in planetary atmospheres. They are formed when a stably stratified layer is disturbed, leaving buoyancy of the displaced air parcel acting as the restoring force of this oscillation (Sutherland, 2010). Being governed by such a fundamental force, they remain an intriguing feature in planetary atmospheres and their role in energy and momentum exchange can be influential in atmospheric circulation (Alexander et al., 2010), which holds particular interest for the case of Venus due to unanswered questions regarding superrotation in the cloud layer (Sanchez-Lavega et al., 2017; Horinouchi et al., 2018).

Different arguments have been made regarding the influence of mesoscale (10–1000 km) gravity waves on the superrotation of the atmosphere. On a planet like Venus, changes in static stability and background wind velocity with height produce processes that modify the propagation of these waves at different altitudes (Hou and Farrel, 1987). These would provoke momentum exchanges between different atmospheric layers which can generally act to reduce the velocity

* Corresponding author.
E-mail address: josesilva@ibs.re.kr (J.E. Silva).

https://doi.org/10.1016/j.icarus.2024.116076
Received 5 November 2023; Received in revised form 29 March 2024; Accepted 1 April 2024
Available online 3 April 2024

difference between the two regions (Sanchez-Lavega et al., 2017). Even though this can imply that gravity waves do not have a large impact on the maintenance of superrotation, their role in the vertical distribution of angular momentum is still uncertain, and they can be one of the elements behind the dynamics of the upper cloud (Horinouchi et al., 2020). Furthermore, the attenuation of waves at different heights, depending on their intrinsic phase velocities, can provide retrograde acceleration (Hou and Farrel, 1987) and friction from momentum deposition which is expected to influence circulation as well. This may elucidate the dynamical conditions in the transition region between the Hadley cell circulation and the sub-solar to anti-solar circulation in Venus' atmosphere (Seiff, 1982; Gilli et al., 2021).

Stationary features interpreted as gravity waves have also been reported, manifesting both on reflected sunlight at ultraviolet (UV) wavelengths (283–365 nm) and on brightness temperature images of the upper cloud at mid-infrared (8–12 μm), further reinforcing a connection between the surface and the cloud layer (Fukuhara et al., 2017; Fukuya et al., 2022; Kitahara et al., 2019; Kouyama et al., 2017; Peralta et al., 2017b). Previous observations of waves in the upper cloud with the Visual Monitoring Camera (VMC) instrument onboard the European Space Agency's (ESA) Venus Express (VEx) space mission showed periodic structures interpreted as gravity waves on the northern hemisphere of Venus, possibly associated with the large *Ishtar Terra* mountain range (Piccialli et al., 2014). Radio occultation data from the Venus Radio Science instrument (VeRa) **on board Venus Express** captured small fluctuations on temperature profiles which were interpreted as gravity waves propagating in the upper cloud (Tellmann et al., 2012).

Gravity waves have also been studied previously at both the upper and lower cloud simultaneously, showing a large diversity of properties and morphologies, unfortunately, limited to the southern hemisphere due to observational constraints (Peralta et al., 2008). A larger survey of gravity waves was made using both data from the Visible and Infrared Thermal Imaging Spectrometer (VIRTIS-M) instrument on VEx and data from the 2 μm Camera (IR2) onboard Akatsuki targeting the lower cloud (44–56 km). The wide range of wave properties suggested different forcing mechanisms, although convection seems the most plausible source for the structures that were characterized (Silva et al., 2021). Higher up in the atmosphere, structures interpreted as gravity waves have also been catalogued from non-LTE (Local Thermal Equilibrium) CO_2 emissions (Garcia et al., 2009).

Given that gravity waves have been detected at several altitude levels, we investigated how their properties might change depending on altitude within the cloud layer of Venus and how transport of these waves might occur between the lower and upper clouds. We use data from the VIRTIS instrument covering the period between August 2007 and October 2008. We present our results of the search and characterization of atmospheric waves interpreted as gravity waves at three slightly different regions in the upper cloud, based on image observations on the dayside at selected wavelengths and sensitive to cloud layers between approximately 60–74 km (Peralta et al., 2017a). In this work, we expand the search of mesoscale waves over previous results obtained in Peralta et al. (2008). Since the period of observations of the upper clouds analysed here overlaps with a previous study of the lower cloud (Silva et al., 2021), we also compare the wave properties on these different altitudes. Additionally, we performed a first inspection of VEx/VIRTIS images at UV wavelengths characteristic of SO_2 absorption (280–320 nm), which allow us to sense altitudes above the top of the clouds (Horinouchi et al., 2018; Machado et al., 2021). We attempt to explore a possible connection between dayside clouds observed at visible/near UV wavelengths (60–74 km) and the nightside opacity patterns captured at infrared wavelengths (44–56 km) (Silva et al., 2021), by searching for wave packets that can be observed at two vertical levels simultaneously, as the single case reported by Peralta et al. (2008).

2. Data acquisition and selection

We used VIRTIS-M on board the Venus Express (VEx) space mission, whose details are presented by Drossart et al. (2007) and Piccioni et al. (2007). Our observations focus on the southern hemisphere due to the high eccentricity of the spacecraft, which leads to high velocities near the pericenter, rendering effective mapping of the disk at these stages challenging (Svedhem et al., 2007).

Given one of our primary goals of this work, this analysis serves as a natural progression from the results presented in Silva et al. (2021), where a systematic search for waves was conducted using the IR channel of VIRTIS-M. In turn, we held similar detection and characterization efforts during the same period, specifically the VEX orbits ranging from 467–921, which roughly corresponds to the time interval between August 2007 to October 2008. During this period we surveyed all available images at four wavelength ranges: 280–320 nm (hereafter, W1) (67–74 km); 365–400 nm (hereafter, W2) (63–70 km); 580–600 and 900–920 nm, both sensitive to the same altitude range (60–65 km), and hereafter referred as W3. The W1 range is mainly sensitive to SO_2 absorption, while also showing reflected light from the top of the clouds, while the W2 range matches the maximum absorption by the unknown UV absorber (Jessup et al., 2015; Perez-Hoyos et al., 2018). The visible range included in W3 shows generally lower contrast features from reflected solar radiation, but at a slightly lower altitude range (Hueso et al., 2015). The near-IR band included in W3 (900–920 nm) was used to complement the data selection procedure since this wavelength region targets approximately the same altitude range (Peralta et al., 2017a). We discuss the altitude of sounded regions at the different wavelength ranges in greater detail in Section 5.1. Thus, by observing wave features at these three **four** wavelength ranges it becomes possible to analyse the impact of waves propagating on the dayside hemisphere of Venus and evaluate their vertical extent and influence on the atmospheric circulation. Even though we were concerned with analysing the same period as in Peralta et al. (2008) and Silva et al. (2021) who examined VIRTIS-IR data, note that the visible channel of VIRTIS was able to provide data for a much longer period than the infrared channel, observing Venus until 2014.

Although the data set used for this work is substantial, even if it represents only a fraction of VEx's mission, the number of images where wave patterns could be recognized was significantly reduced, especially when we consider shorter VIRTIS wavelengths. At wavelengths W1 and W2, about half of the images were either not rendered in a way suitable to our search or were affected by an 'odd-even' defect that produces artificial stripes in the images that interfere with the real waves in the images at small spatial scales. This effect was first observed in ground tests of VIRTIS and it occurs when there are large differences of responsivity between adjacent rows or columns in the detector (Cardesin-Moinelo et al., 2010). Even though this effect is negligible for long exposure times (> 1 s), it becomes significant for shorter exposures and is exacerbated by high-pass filtering which we use to highlight wave features. Images at the W3 range were less affected by this problem, hence both the number of usable images and consequently the number of detected waves increased proportionally, even if the dayside at visible ranges has less contrasting features than W1 and W2 ranges (Hueso et al., 2015; Sanchez-Lavega et al., 2008). Fig. 1 shows an example of this effect.

3. Methods

3.1. Identification of atmospheric waves

The process for wave detection and characterization was similar to what is described in Silva et al. (2021). Since most features have very poor contrast, high-frequency filters are employed to highlight atmospheric features, bringing possible waves to light. To eliminate spurious detections brought by filter artefacts and further enhance

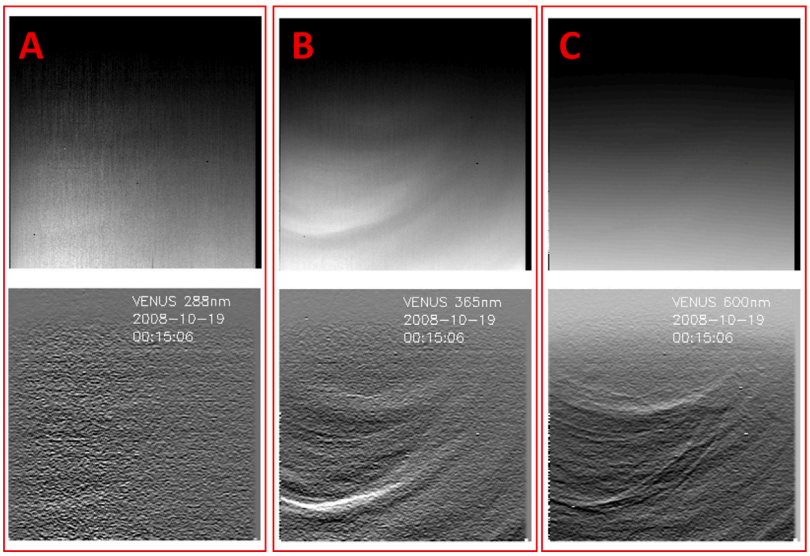

Fig. 1. A VIRTIS-M image at wavelengths W1(A), W2(B) and W3(C) both before and after applying our processing routine. The odd-even effect manifests as set of vertical lines, most recognizable at W1 where creating **creates** stronger noise patterns. With high pass filtering this effect severely affects the visibility of features.

image quality, several neighbouring filters of a VIRTIS cube were stacked (added then averaged) and processed together, along with the verification of consecutive images (separated by the shortest possible time difference) that target the same region of the atmosphere (where possible), to confirm the presence and propagation of the detected waves. To ensure consistency when stacking images at wavelengths W1, W2 or W3, we use the same number of frames for each wavelength range. No photometric corrections or normalization were applied to the images as our main concern was our ability to distinguish contrasting patterns in the atmosphere and most corrections of this kind did not improve significantly the images in our data set.

Each image within the selected period was individually inspected for each wavelength range, looking for alternating contrasting patterns of bright and dark stripes which formed a localized "packet". As a first step to distinguish between possible wave features and other kinds of morphologies, we searched for wave packets with at least three consecutive bright and dark stripes forming a semi-organized wave train observable in the reflected light from Venus' atmosphere.

For both processing and characterization purposes, we made use of the tools provided by the PLIA (Planetary Laboratory for Image Analysis) software (Hueso et al., 2010) as well as other specialized programs designed for Venus image interpretation (Peralta et al., 2018). Multiple examples of detected wave packets at wavelengths W1, W2, and W3 are shown in Fig. 2.

3.2. Characterization of wave properties

A total of 1564 VIRTIS-M-VIS cubes were inspected for this work, and since for each data cube we focused on three wavelength ranges, roughly 4600 images were individually analysed. These images were taken between Venus Express orbit 467 (31st of July 2007) and orbit 921 (27th of October 2008). Navigation of the images (i.e. longitudinal and latitudinal position of each pixel) is provided in geometric cubes, with the data calculated from SPICE kernels. The navigated images can then be projected into cylindrical maps in which longitudes and latitudes are equally spaced facilitating the comparison between images acquired at different times from different perspectives. The following Eq. (1) is used to compute the geometric distance, $Dist$, between two points in the image located at longitudes Λ_1, Λ_2 and latitudes ϕ_1, ϕ_2.

$$Dist = \frac{\pi\sqrt{(\Lambda_2-\Lambda_1)^2 cos^2\left(\bar{\phi}\frac{\pi}{180}\right)+(\phi_2-\phi_1)^2}}{180}(a+h) \quad (1)$$

where $\bar{\phi}$ is the average latitude between measured points, a is the planet radius and h is the altitude of the observed cloud layer. From this calculation, basic morphological properties were measured for each detected packet including horizontal wavelength (λ_x), packet length (PL), and packet width (PW), as illustrated in Fig. 3. Measurements for each of these properties are performed several times for the same packet and then averaged for a more robust characterization.

Orientation with respect to the parallel was also recorded but here we define several orientation types due to the heterogeneous shape of wave packets — crest tilt (θ_T), crest orientation (θ_C) and group orientation θ_G. θ_T is the angle between crest alignment with the equator. θ_C is the orthogonal direction to the crest tilt and is positive when the point of highest longitude is northward and negative otherwise. We define θ_G as the angle between the equator and the general axis that marks the observable length of the packet. This axis can be marked by having the same orientation as the shortest distance between two parallel lines that encapsulate the entire packet. The calculation of each orientation shares the same formula, where $\Delta\phi$ and $\Delta\Lambda$ are the angular difference between the latitude and longitude of points 1 and 2:

$$\theta = arctan\left(\frac{\Delta\phi}{\Delta\Lambda}\right) \quad (2)$$

To aid in the visualization of these definitions of orientation we present a diagram on a wave example in Fig. 3.

For cases where the same wave was observable between consecutive images, we took the opportunity to follow the movement of packets across several images to retrieve the phase velocity of the waves. We used a similar routine as employed in Peralta et al. (2018) to track the displacements of each crest of a wave packet between two images separated by a known time interval, retrieving at least 10 displacement measurements per packet. The local background wind at similar latitudes was also tracked to evaluate the intrinsic phase velocity of these waves and how they relate to the general atmosphere dynamics.

Phase velocities of wave packets and background wind velocity were measured individually using wind tracers and the following equation:

$$U = \frac{cos(\bar{\phi})R_{eq}\frac{\pi}{180}\Delta Lon}{\Delta t} \quad (3)$$

Where U is the zonal velocity of the tracer (phase velocity if wave crests are used as tracers, background wind if other cloud features unassociated with the wave are tracked), $\bar{\phi}$ is the latitude average as in Eq. (1), R_{eq} is the equatorial radius of Venus, ΔLon is the zonal

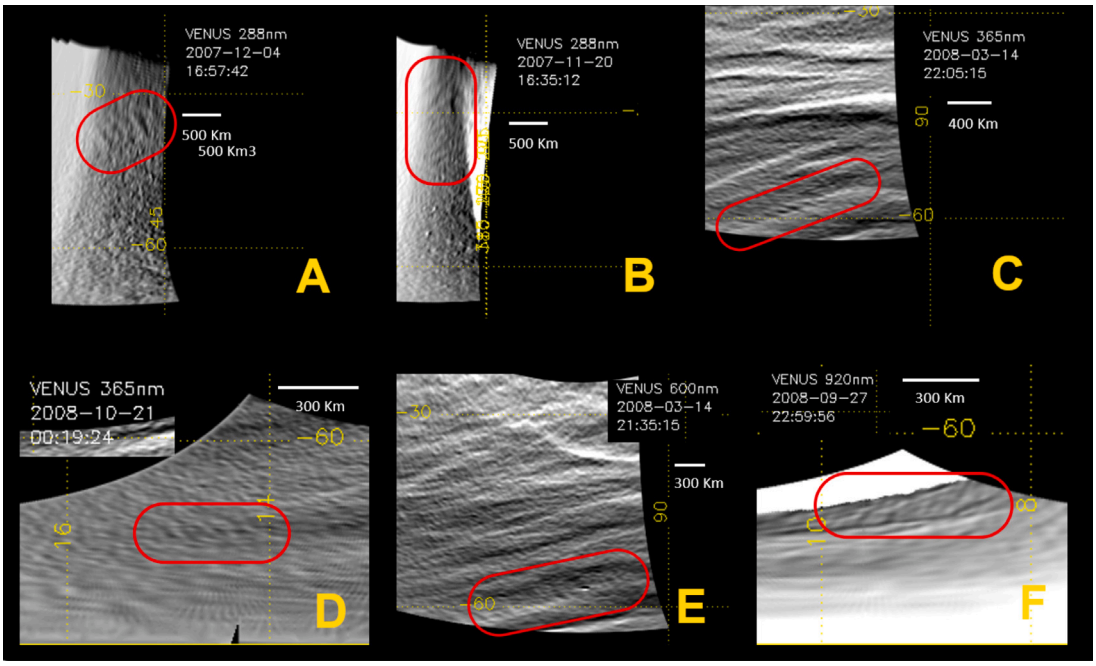

Fig. 2. Wave packets observed on the dayside hemisphere of Venus by VIRTIS-M, highlighted in red. The wavelength range selected is centred on 288 (A–B), 365 (C–D), 600 (E) and 920 (F) nm, with the last two panels assumed to be monitoring the same altitude of Venus clouds. All images where subject to high-pass filtering and contrast enhancement followed by projection. Other wavy patterns present in the examples here are image artefacts and do not represent any atmospheric formation. (For interpretation of the references to colour in this figure legend, the reader is referred to the web version of this article.)

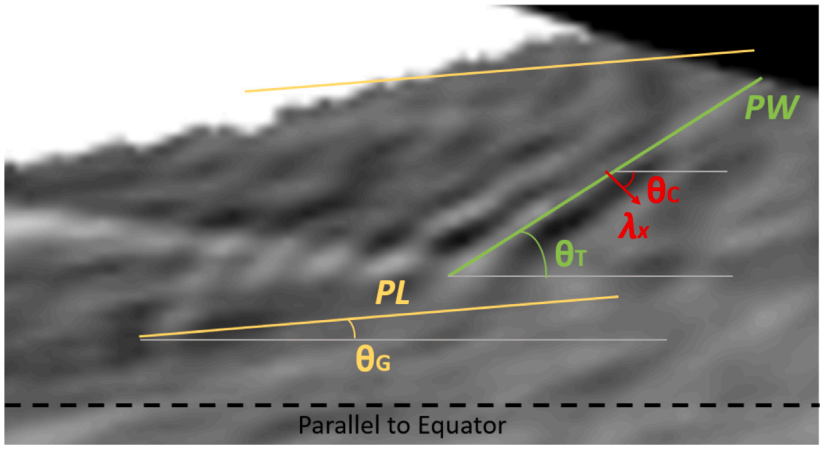

Fig. 3. A diagram of the measurement routine for morphological characterization. The red, green and yellow coloured lines represent how the horizontal wavelength (λ_x), packet width (PW) and packet length (PL) are measured respectively. The angles θ_T, θ_C and θ_G illustrate the crest tilt, crest orientation and group orientation, all relative to the parallel. (For interpretation of the references to colour in this figure legend, the reader is referred to the web version of this article.)

displacement of the tracked feature between images A and B and Δt the temporal interval between the images. Wave phase speed is measured by tracking individual structures that belong to the wave packet (usually wave crests) between one or more pairs of images, depending on the lifetime and visibility of the packet. Given the observational constraints brought by VEx's orbit around Venus, usually, the same region of the atmosphere could only be monitored for consecutive periods no longer than 6 h, which only allows for a minimum lifetime of the wave's propagation to be observed in this way.

3.3. Other wave properties

If we assume that the wave packets that were detected in this analysis correspond to atmospheric gravity waves, additional properties can be inferred by applying simple analytical models. Using linear theory to describe wave phenomena, neglecting effects from Venus' rotation and assuming a *Boussinesq* flow, we can describe gravity waves as a small perturbation on the mean flow at a specific atmospheric level while considering the local pressure of the layer constant except when coupled with gravity (Nappo, 2002; Holton, 2004; Sutherland, 2010; Sanchez-Lavega, 2011; Peralta et al., 2014). Thus, an oscillatory disturbance caused by the buoyancy of neighbouring layers when subject to these small perturbations can be represented by the dispersion relation, which provides a relationship between a wave's phase speed and its wavenumber:

$$(c_p^x - \bar{u})^2 = \hat{c_p^x}^2 = \frac{N^2 + \xi^2(m^2 + \frac{1}{4H_z^2})}{k^2 + m^2 + \frac{1}{4H_z^2}} \tag{4}$$

Where c_p^x is the zonal component of the phase velocity, $\bar{u}$ is the average zonal wind, N is the *Brunt-Väissälä* frequency, k and m are the horizontal and vertical wave-numbers, H_z represents the density

scale height at altitude z and ξ accounts for the centrifugal force when modified by the meridional shear of the background wind (Schubert and Walterscheild, 1984; Peralta et al., 2014). Note here that we reduce absolute phase velocity to the intrinsic phase velocity of the waves ($\hat{c_p^x}$) by subtracting the contribution from the background flow. We do not include the meridional component of the phase velocity as its contribution to Venus' circulation is limited when compared to the zonal flow and more importantly, because the best spatial resolution achieved on these images is often comparable with the absolute values measured for the meridional wind, possibly leading to unreliable results (Hueso et al., 2012, 2015). The *Brunt-Väissälä* frequency can be estimated using the results from radio occultation measurements described in detail in Ando et al. (2020), namely temperature and consequent static stability vertical profiles for the upper/middle clouds:

$$N = \sqrt{\frac{g.S}{T}} \tag{5}$$

Where S is the static stability, g is the acceleration of gravity and T is the atmospheric temperature. As both S and N vary with altitude and latitude range, multiple values were calculated for each variable. For the latitude range, we considered the intervals suggested by Ando et al. (2020) based on the distributions of zonally and temporally averaged temperatures and static stability. Regarding altitude ranges we considered the definitions summarized in Peralta et al. (2017a) for the wavelength ranges addressed in this work (W1, W2 and W3). We discuss this topic in greater depth in Section 5.1. The estimation of the *Brunt-Väissälä* frequency is then used to calculate the vertical wavelength of characterized packets. Considering the horizontal and vertical wave-numbers and their relationship with wavelength:

$$k = \frac{2\pi}{\lambda_x} \qquad m = \frac{2\pi}{\lambda_z} \tag{6}$$

Where λ_x and λ_z are the horizontal and vertical wavelengths of packets and introducing these in Eq. (4) we can compute the vertical wavelength of wave-packets with:

$$\lambda_z = \frac{2\pi\sqrt{\hat{c_p^x}^2 - \frac{\xi^2}{k^2}}}{\sqrt{N^2 - \hat{c_p^x}^2 k^2 - \frac{1}{4H_z^2}\left(\hat{c_p^x}^2 - \frac{\xi^2}{k^2}\right)}} \tag{7}$$

Since this value is sensitive to the *Brunt-Väissälä* frequency, it is influenced by latitude and altitude range. Further up in Section 5.1.4 we will also discuss the influence of vertical shear of the zonal wind for wave packets with retrieved phase velocities.

3.4. Considerations on sources of uncertainty

For both detection and characterization purposes, the spatial resolution of images in the data set is the most important factor when considering uncertainty since it affects the ability to see wave structures in the first place and also is the main contributor to error in distance measurement for various morphological parameters. Table 1 shows the average spatial resolution of images (δ_{Dist}) on the regions where waves were identified. It also shows the average uncertainties for each measured wave property (in square brackets), influenced mainly by spatial resolution and the processing applied to each image, to a lesser degree. Given the smaller sample in W1, the measurement uncertainties across packets are larger. Since the spatial resolution is the most limiting factor in measuring wave properties, the fact that the mean uncertainties $\zeta_{\lambda_x}, \zeta_{PW}$ and ζ_{PL} are comparable with the spatial resolution at the wave's region is expected. However, this is less valid for waves in W1 due to the smaller sample size.

Regarding the variations between distinct wave packets, we can see from the standard deviations from the average value of each property in Table 1 that values for PW and PL can change considerably between different packets, signalling diversity in waveforms. Also notice the spread of group orientations and crest tilt angles when compared with their mean values as illustrated in Table 1, although the limited number of detected waves at W1 somewhat influences the results presented here.

Regarding phase velocities, not only is spatial resolution a factor in determining uncertainty on the wind tracers but the time interval between images as well:

$$\delta U = \frac{\delta_s}{\Delta t} \tag{8}$$

Where δU is the velocity error, δ_s is the spatial resolution on the wave packet region, and Δt is the time interval between images in the pair used to retrieve wind tracers. It is obvious from Eq. (8) that larger temporal differences between images lead to smaller errors. The mean error for the wind tracers across all dynamically characterized packets was approximately 10 m/s.

Another limiting factor concerning wave detection was related to the overall quality of the images. Since we chose the period of observation to overlap with Silva et al. (2021) which focused on the nightside, a non-negligible part of the data set for the visible channel of VIRTIS does not show reflected light, making such images unsuitable for this work. Also, even though Venus' atmosphere shows overall less contrast at visible wavelength (Hueso et al., 2012), these were the most reliable wavelengths to detect and characterize waves. A possible reason for this situation is the influence of the before-mentioned non-uniformity response of the detector which is more significant at shorter wavelengths and short exposure times.

Finally, uncertainties in the geometrical information and timing of the images are estimated to cause navigation errors smaller than 1 km and do not play a significant role in this analysis.

4. Results

A total of 69 wave packets were characterized this way across wavelengths W1, W2 and W3. At W1, the odd-even effect was strongest and only 4 detections were confirmed during this period. For W2, 14 images with waves were identified and W3 holds most of the detections with 51 observations.

At least 20 of the images with a packet share the same wave formation across wavelength ranges. Two cases with the same packet at W1 and W2 wavelengths, 15 cases with the same packet at W2 and W3 wavelengths, and three cases where the same packet could be seen across the three wavelength ranges. However, note that due to the before mentioned odd-even effect, it becomes challenging to confirm at the wavelength ranges W1 and W2 the simultaneous existence of wave features observed in W3 when exposure times are short (< 1 s).

The same wave structure can also be observed in consecutive images, thus the total number of detections when referring to wave packets detected might be misleading. As such, we define a distinct wave packet as an independent feature that can be observed on multiple images but has singular coordinates and characteristics. Taking all repeated waves we arrive at 41 characterized distinct waves. As stated in Section 3, consecutively observed packets made their dynamical characterization possible. A total of 16 distinct packets were tracked for their phase speed and approximate trajectory in the atmosphere of Venus.

4.1. Wave properties

In Fig. 4 we show the characterized wave packets at W1, W2 and W3. Some of these overlap because the same wave was visible at multiple wavelengths. Since VIRTIS observations during the selected period were not uniform over all geographical locations of Venus we calculated the ratio of detection of waves to the total number of observations for a specific area of the planet, which we show in Fig. 5. The size of the area used in the calculation of the wave occurrence maps is a square area with 10° latitude and 20° longitude, centred on the wave's mean position. Our study is focused on the southern

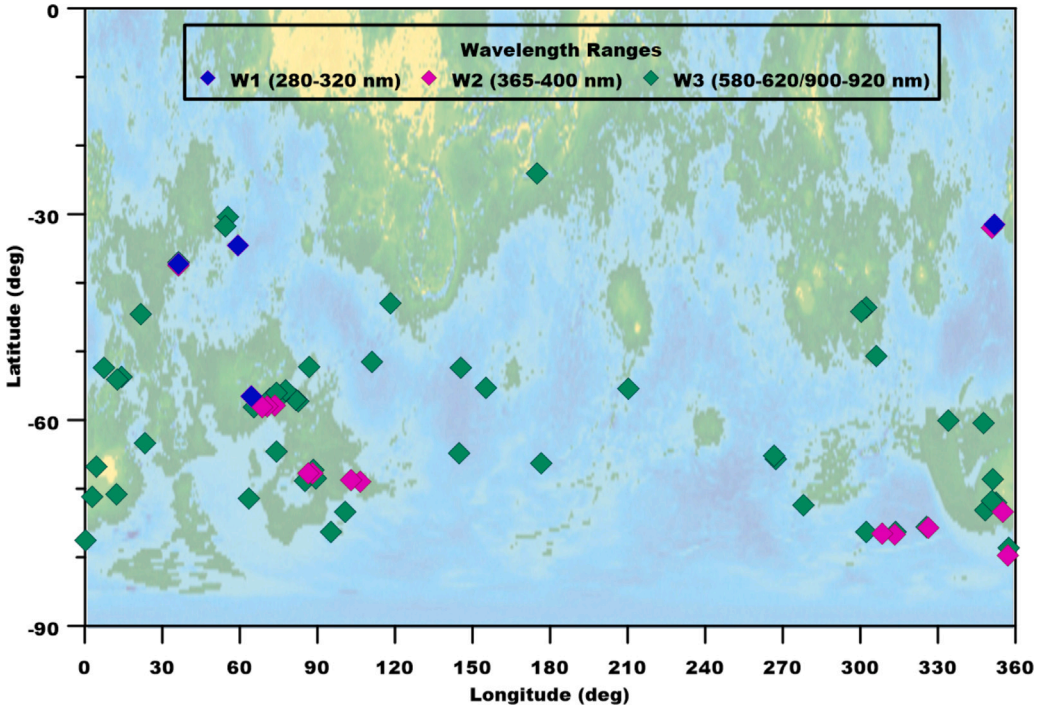

Fig. 4. Distribution of all characterized wave packets between August 2007–October 2008 over the topography of Venus. Dark blue data points represent the detections in W1, magenta in W2 and green in W3. Topographical data was extracted from Magellan data. (For interpretation of the references to colour in this figure legend, the reader is referred to the web version of this article.)

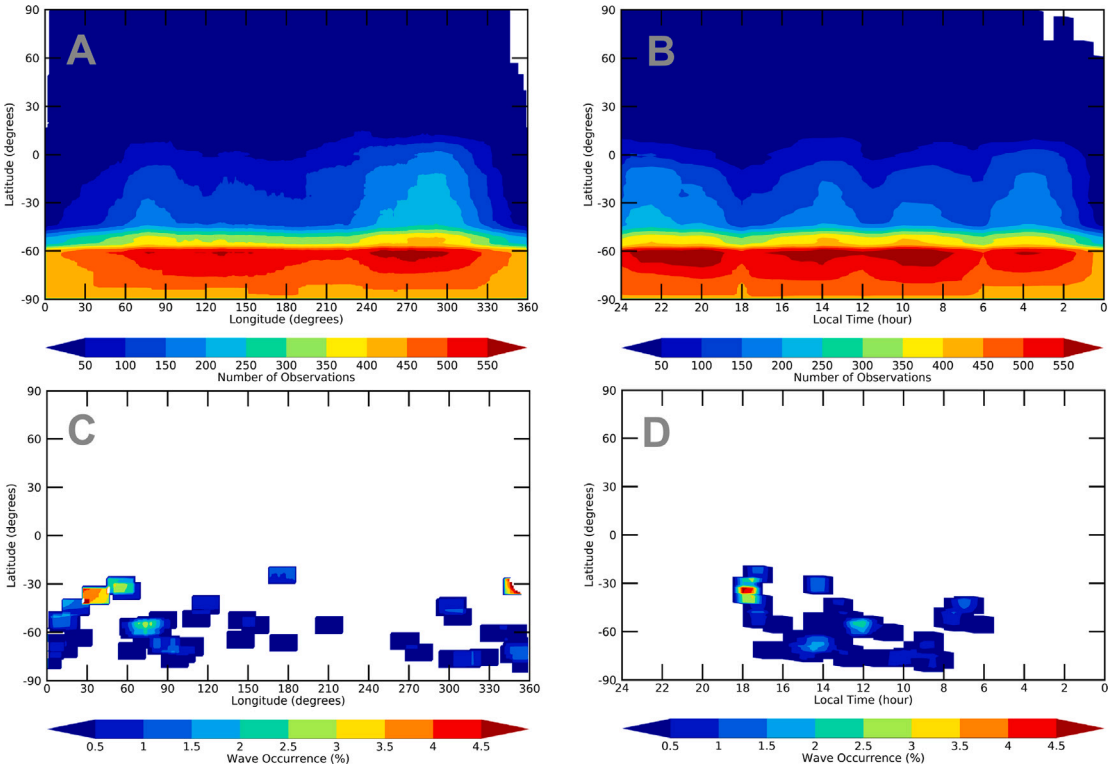

Fig. 5. *Top:*Latitude-Longitude (A) and Latitude-Local Time (B) coverage maps for VIRTIS-M-VIS observations during the selected period of observation. *Bottom:*Wave frequency maps for Latitude-Longitude (C) and Latitude-Local Time (D), showing the distribution and occurrence of wave packets. The size of the bins in the wave occurrence maps is 10° latitude by 20° longitude centred on the waves mean position. White space signifies lack of data.

Table 1
Morphological Properties of wave packets. For each wavelength range ([λ]) we list the number of characterized packets in parenthesis. λ_x is the horizontal wavelength, PW is the packet width, PL is packet length and θ is the orientation of the packet. Each table entry in λ_x, PW, PL is the mean value **for that property for packets characterized at that wavelength**. θ_G is the group orientation, θ_T is the crest tilt and $\|\theta_G - \theta_C\|$ is the angle between the crest and group orientations, henceforth referred to as *crest skew*. Standard deviations of each morphological property are represented next to the average value. Below in square brackets we represent the measurement uncertainty of each morphological property for individual packets, since each packet's properties are measured several times.

[λ]	δ_{Dist}	$\lambda_x \pm \sigma_{\lambda_x}$ [ζ_{λ_x}]	PW $\pm$ σ_{PW} [ζ_{PW}]	PL $\pm$ σ_{PL} [ζ_{PL}]	$\theta_G \pm \sigma_{\theta_G}$ [ζ_{θ_G}]	$\theta_T \pm \sigma_{\theta_T}$ [ζ_{θ_T}]	$\|\theta_G - \theta_C\|$
(nm)	km/pix		(km)			(°)	
W1 (#4)	32.0	211 ± 47 [30]	516 ± 159 [94]	939 ± 567 [58]	3.9 ± 61.9 [3.2]	−27.3 ± 47.9 [6.0]	13.8
W2 (#14)	23.4	122 ± 56 [19]	264 ± 188 [35]	468 ± 338 [35]	1.8 ± 25.3 [2.6]	−14.0 ± 47.9 [7.4]	34.5
W3 (#51)	22.6	107 ± 48 [17]	289 ± 163 [35]	405 ± 213 [29]	3.9 ± 17.1 [2.7]	−11.3 ± 56.5 [5.2]	23.2

hemisphere due to the apocenter of Venus Express' orbit close to the south pole (Titov et al., 2006).

In general, wave occurrence is less than 5% (Fig. 5), and wave activity seems to be concentrated close to the evening terminator at local times between 17–18 h. However, caution must be taken when extracting conclusions since this low recurrence might be partially caused by the problem of low contrast in VIRTIS-M images.

4.1.1. Morphology

For characterization, our first step was to measure the basic properties of detected wave packets. In Table 1 we list the basic morphological properties of the characterized packets for each wavelength range ([λ]) along with the average spatial resolution (δ_{Dist}) of images at each wavelength range. We include here spatial properties like horizontal wavelength, packet width and length and several orientations including the *crest skew*. This last orientation parameter can be seen as an indication of wave deformity from a 'standard shape' where crests are perfectly perpendicular to the group's orientation. For each wavelength range, we also note its respective number of characterized packets.

Also in Table 1 we show the standard deviations of wave packet dimensions from the mean values. Since several measurements of the same property are taken for a single wave packet, it is also useful to verify that the retrieved measurements are consistent within the same wave packet. On the same table the uncertainties associated with the measuring procedure for each property are written in square brackets. Even though most of the waves detected during this period have scales of hundreds of km, and despite the high spatial resolution at sub-spacecraft point for most of our images (~ 20 km/pix) it is possible that smaller packets also manifest at these wavelengths, similar to what has been reported in Piccialli et al. (2014). Another point to consider is that some of these packets were detected close to the evening terminator, where visibility becomes limited at these wavelengths. As such, the packets in question might be larger (in PW or PL) and for those, we can only provide a minimum value for both wave dimensions. Figs. 6 and 7 show how the measured properties of the waves in this study change with latitude and local time. Although most of the waves are located southward of 50°, the dimensions of wave packets seem to subtly rise as they approach the equator. Changing circulation regimes for higher latitudes (close to the "cold collar") might disturb the formation mechanisms for larger wave structures or aid in their destruction. Alternatively, the cold collar marks the transition from elevated clouds observed in UV to lower clouds descending over 10 km from 74 km in subpolar latitudes to about 65 km around the inner side of the cold-collar (Ignatiev et al., 2009). These large changes in altitude may occur through vertical layers of the atmosphere in which the stability properties change strongly, modifying the conditions for wave propagation. A simpler explanation may reside in the general fact that for VIRTIS-M data, the spatial resolution becomes larger for equatorial latitudes, explaining a lack of smaller wave packets.

Another tentative remark concerns the tendency for group orientation to align with parallels, even though the background zonal wind is generally weaker, south of 60°. The measured properties seem to be more influenced by local time. There is some indication that waves' spatial scales are enhanced close to the evening terminator, with the group orientation also seemingly affected.

Table 2
Intrinsic Phase Velocity of Dayside Waves with VIRTIS-M.

VEx Orbit	Lat (°)	LT (h)	$\hat{c_p^x}$ (m/s)	$\delta_{\hat{c_p^x}}$ (m/s)
694 (W2)	−58.4	12.4	−12	9
477 (W2)	−69.6	13.4	−16	12
698 (W3)	−31.1	14.2	−6	18
468 (W3)	−52.3	12.8	−15	3
650 (W3)	−53.3	7.2	5	6
694 (W3)	−57.3	11.9	−13	9
740 (W3)	−63.9	8.4	−23	8
914 (W3)	−65.9	14.1	22	7
476 (W3)	−66.6	15.0	−11	14
476 (W3)	−68.4	14.4	−12	11
891 (W3)	−70.4	8.9	−2	7
912 (W3)	−72.5	14.6	−9	7
479 (W3)	−72.8	16.6	18	11
471 (W3)	−74.8	12.7	−1	4
880 (W3)	−76.2	10.7	−39	7
885 (W3)	−78.3	8.3	15	7

4.1.2. Dynamics — phase velocity

For the 16 cases where waves were tracked in sequences of several images, we retrieved the phase velocity of the packets by tracking the movement of wave crests at different times during the observed propagation. The method employed here has many similarities with cloud tracking which has been used extensively to study Venus' cloud deck (Goncalves et al., 2019; Hueso et al., 2015; Machado et al., 2017). We could not find any example of an image sequence where the dynamics of a wave at W1 could be tracked. Hence, no dynamics data for these packets was retrieved. Fig. 8 shows the retrieved phase speed velocities of 16 wave packets that could be tracked within the observation period. For comparison, we also show the average zonal wind profile obtained by Hueso et al. (2015). Most of the packets follow the average zonal wind profile or move within the boundaries of the errors. However, some wave packets show considerable deviations from this mean flow. Such deviations can be expected since considerable variety in the instantaneous values of the zonal wind with longitude, local time, and period of observation has been reported (Machado et al., 2021; Sanchez-Lavega et al., 2017).

For a clearer picture of the waves' motions in the atmosphere, we subtract the local background wind, retrieved at the same latitude level by tracking cloud features not related to the wave propagation. Table 2 shows the values for the intrinsic phase velocity of waves, where negative velocities imply waves being faster than the background wind since the general zonal circulation on Venus is retrograde. Almost all of the waves dynamically characterized display such values in relation to the background wind, with one case going at speeds that

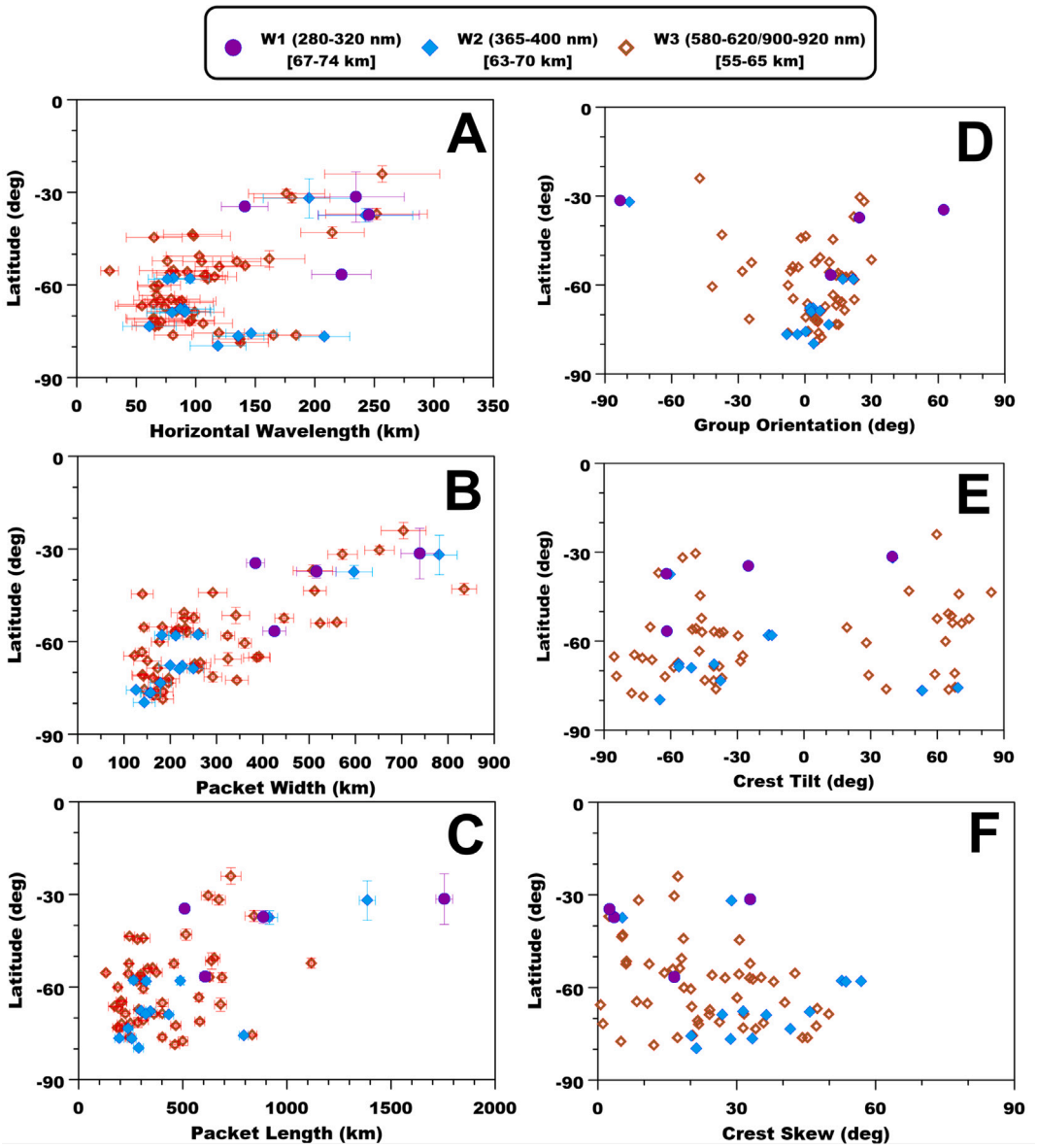

Fig. 6. Morphological properties (A: Horizontal Wavelength, B: Packet Width, C: Packet Length, D: Group Orientation, E: Crest Tilt, F: Crest Skew) with respect to the packet's latitude on Venus. We ignore the northern hemisphere due to orbital constraints. Packets are also separated in wavelength range showing W1 detections in purple, W2 in blue and the W3 range in red. Approximate altitude ranges for each wavelength range is also represented in square brackets. For orientation parameters we do not include the error bars here because the errors are associated with the spatial resolution (in degrees) which for all cases is less than 1 deg/pix. (For interpretation of the references to colour in this figure legend, the reader is referred to the web version of this article.)

are almost 40 m/s greater than the surrounding winds. The error $\delta_{c_p^x}$ is based on the image's spatial resolution and time interval between them as explained in Section 3.4. Most of the waves were tracked over a relatively short period (approximately 1 h) as shown in Fig. 9 and their trajectory suggests that they mostly follow the zonal direction, possibly because the zonal wind dominates atmospheric circulation in the cloud deck (Sanchez-Lavega et al., 2008). As previously mentioned, the starting and end positions for the waves represented in this work are not directly related to wave generation or dissipation since we were limited by the observing conditions brought by VEx's orbit around Venus.

4.1.3. Dynamics — vertical wavelength

Table 3 shows the calculated values of the vertical extent of the waves using Eq. (7). For each distinct packet, we list the calculated value of the vertical wavelength (λ_z) along with the propagated error

Table 3
Vertical Wavelengths for dayside wave packets detected with VIRTIS-M-VIS.

VEx Orbit	Lat (°)	LT (h)	λ_z (km)	δ_{λ_z} (km)
694 (W2)	−58.4	12.4	4	3
477 (W2)	−69.6	13.4	5	4
698 (W3)	−31.1	14.2	2	7
468 (W3)	−52.3	12.8	6	2
650 (W3)	−53.3	7.2	2	2
694 (W3)	−57.3	11.9	5	4
740 (W3)	−63.9	8.4	7	6
914 (W3)	−65.9	14.1	7	5
476 (W3)	−66.6	15.0	3	5
476 (W3)	−68.4	14.4	4	4
912 (W3)	−72.5	14.6	1	2
479 (W3)	−72.8	16.6	5	5
880 (W3)	−76.2	10.7	11	7
885 (W3)	−78.3	8.3	4	3

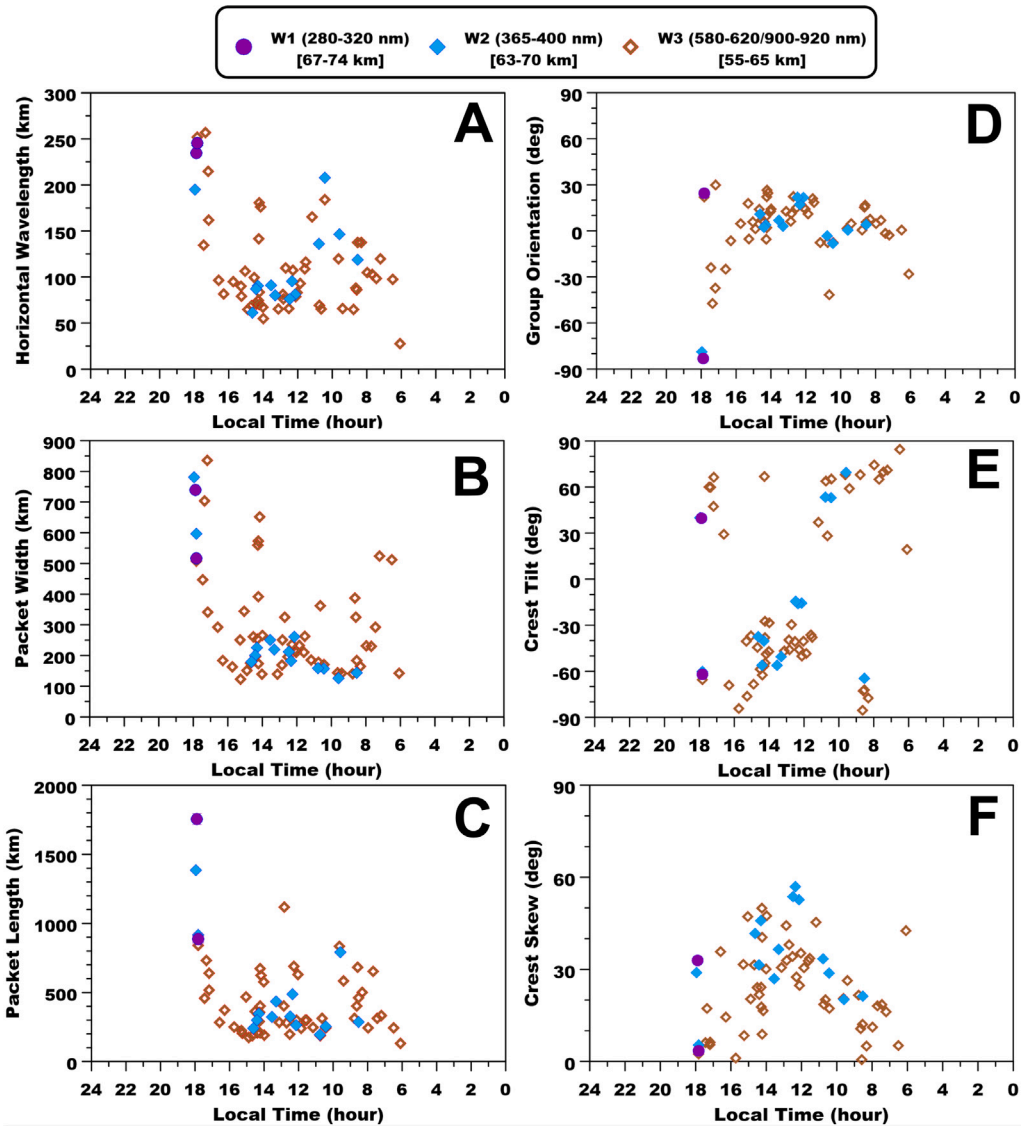

Fig. 7. Morphological properties versus their Local Time coordinate. Organization of panels is identical to Fig. 6. The morning and evening terminators are approximately at 7–8 h and at 18–19 h. The errors on local time are generally less than 0.5 h, which makes them comparable to the size of the symbols illustrated here. The errors associated with morphological parameters are identical to what is presented in Fig. 6.

δ_{λ_z} which was calculated with the following equation:

$$\delta_{\lambda_z} = \sqrt{\left(\frac{\partial\lambda_z}{\partial c_p^{\hat{x}}}\right)^2 \delta c_p^{\hat{x}} + \left(\frac{\partial\lambda_z}{\partial k}\right)^2 \delta k + \left(\frac{\partial\lambda_z}{\partial N}\right)^2 \delta N + \left(\frac{\partial\lambda_z}{\partial H_z}\right)^2 \delta H} \quad (9)$$

As expected, the biggest contributors to the propagated error of the vertical wavelength were the retrieved phase velocities and the *Brunt-Väissälä* frequency.

From these results, we observe that the vertical extent of waves is rather small when compared with their morphological properties (see Table 1). As demonstrated by Ando et al. (2020), static stability can vary significantly with latitude and altitude, which plays a role in the calculation of vertical wavelength via the *Brunt-Väissälä* frequency (see Eq. (7)). However, static stability profiles can be generalized for specific latitudinal ranges, namely the equator (0°–30°) and mid-latitudes (30°–60°), while for higher latitudes, narrower ranges become necessary. This generalization is possible since within these latitude ranges the static stability has been observed to not change considerably at the altitudes studied in this work. Even though we calculated the value of λ_z for each altitude between 60–74 km, with 1-kilometre bins, we also defined altitude intervals for each wavelength window: W2 - 63–70 km, W3 - 61–65 km. We can then average the *Brunt-Väissälä* frequency values for each altitude level within range at the appropriate latitudinal window (depending on the wave location) to arrive at the vertical wavelength values in Table 3.

Even though this simple approach is powerful enough to calculate approximate values of the vertical wavelength, using the aforementioned approximations, it does not capture the influence of the vertical shear of the background zonal wind. Since the zonal wind is dominant on the cloud layer of Venus, it can have a significant impact on wave propagation. We approach this influence in Section 5.1.4 with a recalculation of the vertical wavelength using a more sophisticated model.

5. Discussion

5.1. Altitude of waves within the cloud layer

The observation of Venus' atmosphere at different wavelengths enables the monitoring of multiple levels of the atmosphere, taking advantage of several ongoing processes. The wavelength range used in this work is concerned with the reflection or absorption of sunlight on

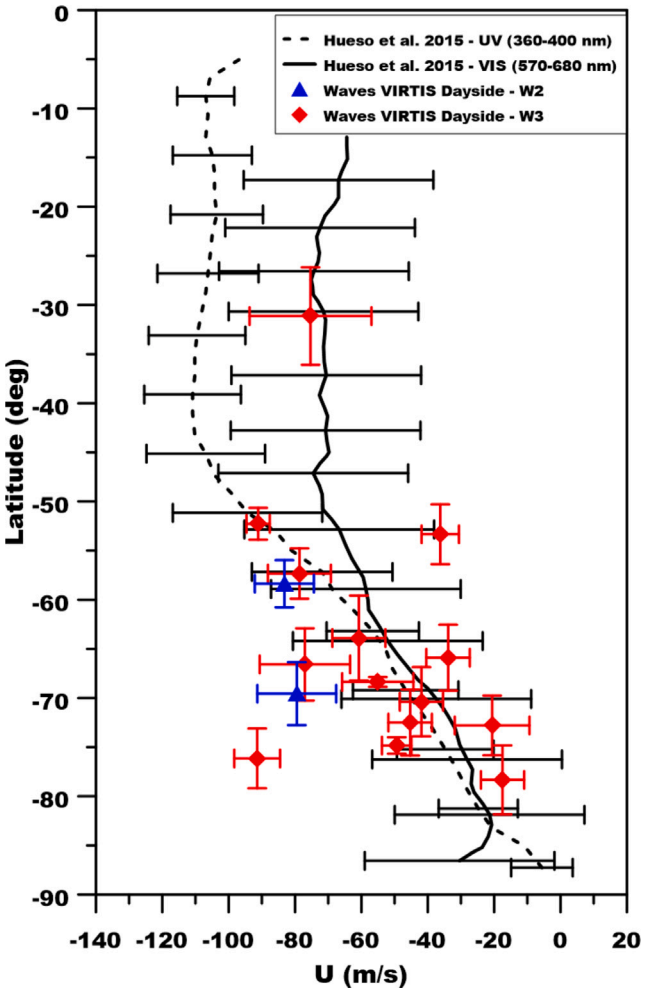

Fig. 8. Retrieved phase velocities of distinct wave packets within our observing period. Here we distinguish between waves observed at W2 and W3 ranges, whose correspondent average wind profiles are different. The dashed and filled zonal wind profiles are an average of six years of Venus observations at UV and visible wavelengths respectively (Hueso et al., 2015).

the dayside. Inferred parameters that can be determined from observations at these wavelengths like dynamics, composition, and thermal structure, can be used to inform their vertical distribution (Peralta et al., 2017a; Sanchez-Lavega et al., 2008; Titov et al., 2018).

Multiple previous studies (Cottini et al., 2015; Hueso et al., 2012, 2015; Ignatiev et al., 2009) have explored some of these processes to determine the location of observable features at different wavelengths and the altitude of the cloud tops, with particular emphasis on the ultraviolet range, where dayside images exhibit highly contrasted cloud patterns whose shape is variable within the time scale of several hours. This is opposed to visible wavelengths where the atmosphere of Venus shows a much blander appearance (Hueso et al., 2015; Peralta et al., 2007; Sanchez-Lavega et al., 2008).

5.1.1. Observed wavelength ranges analysis

Regarding the observing wavelength ranges used in this work (W1, W2, and W3), we consider the altitude estimations that have been presented in the literature, which tentatively establish that each of these ranges sounds at slightly different altitude levels.

For W1, measurements of both mean and instantaneous wind speeds, Horinouchi et al. (2018) and Machado et al. (2021) have shown a difference in 10–15 m/s on the wind profile between W1 and W2 observations, which supports a difference of ∼ 4 kilometres between

Table 4
Summary of the approximate altitude windows on Venus where each observing wavelength range sounds in the atmosphere.

Wavelength Range (nm)	Altitude Range (km)	References
W1	67–74	Machado et al. (2021), Perez-Hoyos et al. (2018)
W2	63–70	Cottini et al. (2015), Ignatiev et al. (2009), Jessup et al. (2015)
W3	55–65	Hueso et al. (2015), Peralta et al. (2019), Sanchez-Lavega et al. (2008)

regions sounded at each of these wavelengths. This is consistent with recent numerical global circulation modelling results (Gilli et al., 2020; Takagi et al., 2018). However, since the SO_2 vertical distribution is quite variable and it is the main absorber in the W1 range (Lee et al., 2022; Marcq et al., 2013, 2020), this altitude difference between levels sounded at W1 and W2 is not well constrained.

A plethora of previous studies have been dedicated to the wavelength range encompassed by W2, particularly due to the high contrasting features from UV absorption which enable reliable dynamical studies via cloud tracking methods (Hueso et al., 2012, 2015; Horinouchi et al., 2018). Coupled with previous works on the altitude of the cloud tops (Cottini et al., 2015; Ignatiev et al., 2009), there is moderate consensus that this wavelength range monitors clouds at the altitude range between ∼ 63–70 km. Following this assumption and the results by Machado et al. (2021), we can place the region sounded by W1 a few km higher than W2.

Different cloud features can be observed at visible wavelengths than at the UV, and it is generally accepted that the region observed with the W3 range lies deeper than the level where contrasting UV features are observed (Sanchez-Lavega et al., 2008; Hueso et al., 2015). The vertical profile of the zonal wind represented in Fig. 10 also shows that the wind speed can change significantly within the possible different altitude ranges considered, especially concerning the difference between the region sounded at W1–W2 and W3. The exact vertical difference between the two observing ranges is not well constrained though, with differences ranging between 4 and 12 km below the top of the clouds observed at ultraviolet wavelengths (Peralta et al., 2019). We present in Table 4 a summary of approximated altitude ranges surveyed by each wavelength range discussed in this section.

Despite the differences in dynamical profiles shown concerning wavelengths W1, W2, and W3, the inferred wave properties do not seem sensitive to these changes. However, we acknowledge that our data set is dominated by observations at W3, thus drawing firm conclusions on the influence of altitude on the morphological and dynamical parameters of the waves characterized here can be difficult.

5.1.2. Wave packets at multiple levels

A more concerning aspect is the visibility of waves at each wavelength range. As noted by the distribution of characterized waves in Fig. 4 a significant number of wave detections presented in this work are based on data with short exposure times (< 1s). This leads to possible ambiguity in claiming that waves observed on many images at W3 are not present at W2, where they may be obscured by image defects. We verified that in only one case we can make this claim with confidence due to the larger exposure time of the image. The reverse is also true in a few cases, with packets being observable at W1 or W2 exclusively despite shorter exposure times. Examples of these cases are illustrated in Fig. 11.

The estimated vertical extension of the dayside waves can also be an indicator of the presence of waves at the altitudes simultaneously sounded in images in the W2 and W3 wavelength ranges since the

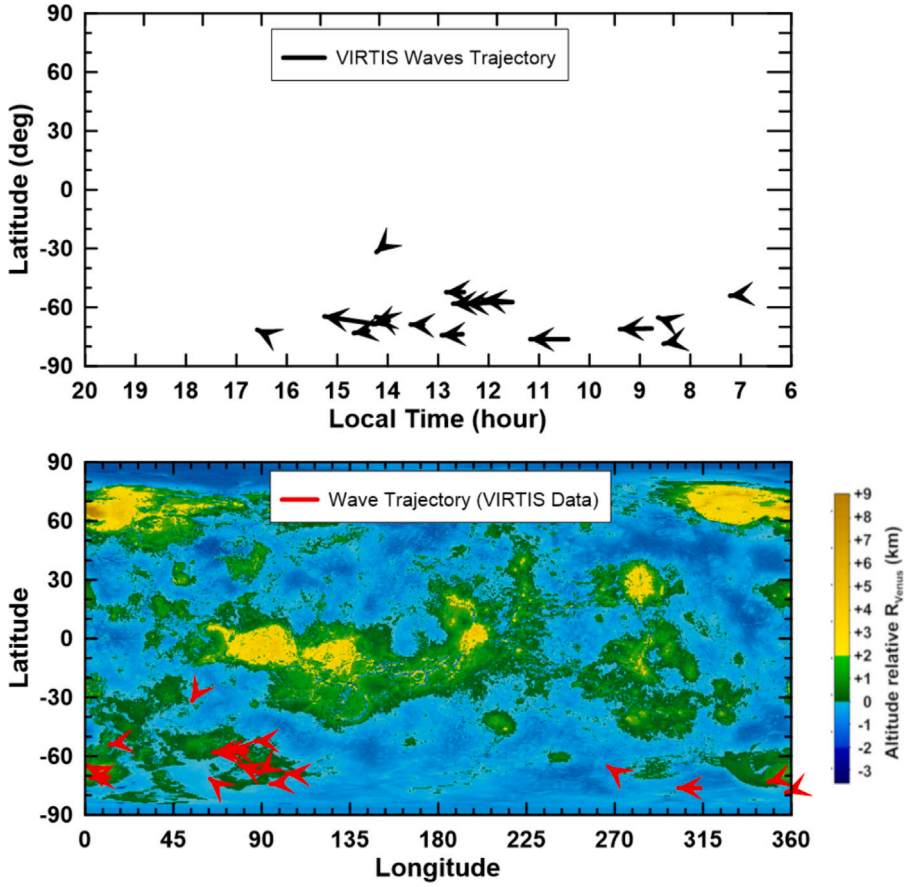

Fig. 9. Observed propagation direction of tracked distinct wave packets in longitude/latitude and local time/latitude. The arrows point to the direction of propagation of the wave. Observed lifetime of packets is between 0.5 – 3 h.

vertical distance between these locations in the cloud layer is comparable to the calculated vertical wavelengths. There are examples in this dataset where waves visible at W2 and W3 have vertical extensions large enough so that it would be possible to observe them on both wavelength ranges. However, we could not confirm this for all cases where the vertical wavelength was also enough to make waves appear at both levels.

5.1.3. *Influence of altitude in vertical wavelength estimation*

The different altitudes that can be considered for the detected waves play a significant role in the calculation of vertical wavelengths, due to changes in the static stability profile with altitude. According to the temperature profiles based on radio occultations experiments performed by Akatsuki and retrieved by Ando et al. (2020), the static stability rises steeply from 60 km of altitude until a peak is reached close to 65 km from which it descends smoothly within the remaining cloud deck. This sharp rise is stronger polewards of 60° latitude although with substantial errors. This leads to larger uncertainties on the vertical wavelength of waves when considering altitudes lower than 65 km, which can be a possibility for the W3 waves at mid-high latitudes. We verified how the vertical wavelength varies with the altitude considered in the calculation, finding that their values stabilize from 61 km upwards. As such, for vertical wavelength calculation for the altitude range corresponding to W3, we considered altitudes between 61–65 km, from which the average values of λ_z are expressed in Table 3 calculated with Eq. (7).

5.1.4. *Influence of wind shear*

The base calculation of vertical wavelength (Eq. (7)) does not take into account the influence of vertical wind shear, which can impose limits on wave propagation or distort wave shapes. However, vertical wind shear of the zonal wind within the cloud deck must be present considering the differences in wind profiles at different altitudes. This effect is strongest at latitudes $< 55°$ with wind speed variations of around 8 m/s for every kilometre risen in the atmosphere on the upper cloud as reported in Sanchez-Lavega et al. (2008) and expanded upon by Hueso et al. (2015). Other observations and models of Venus' atmosphere point to less vigorous vertical wind shear (3–6 m/s per km in the upper cloud), although all agree with decreasing wind shear at poleward latitudes (Peralta et al., 2014; Lefèvre et al., 2018).

A method to evaluate if the wind shear has an impact on the gravity waves' propagation is to verify whether the waves are fast enough to avoid perturbation from the variation of wind speed with height within the boundaries of the vertical wavelength (Iga and Matsuda, 2005). For the waves reported here, we applied the relationship $c_p^{\hat{x}} > \lambda_z |\frac{\partial \bar{u}}{\partial z}|$, concluding that wind shear should be considered in the calculation of vertical wavelength for most packets.

Thus a recalculation of λ_z was required using a textbook solution to the perturbation theory for gravity waves which applies the WKB approximation (Nappo, 2002):

$$m^2(z) = \frac{N^2}{c_p^{\hat{x}2}} + \frac{\partial^2 \bar{u}}{\partial z^2}\frac{1}{c_p^{\hat{x}}} - \frac{1}{Hc_p^{\hat{x}}}\frac{\partial \bar{u}}{\partial z} - \frac{1}{4H^2} - k^2 \tag{10}$$

Table 5 shows the estimated values of vertical wavelengths calculated with Eq. (10) ($\lambda_z(WS)$), approximated to the same order of magnitude as the largest errors ($\delta_{\lambda_z(WS)}$). Interestingly, if we consider only altitudes above 61 km, the relative difference between vertical wavelengths calculated with and without wind shear is mostly below 10% for most packets when taking wind shear values from previous space-based observations (Peralta et al., 2014). However, if we consider

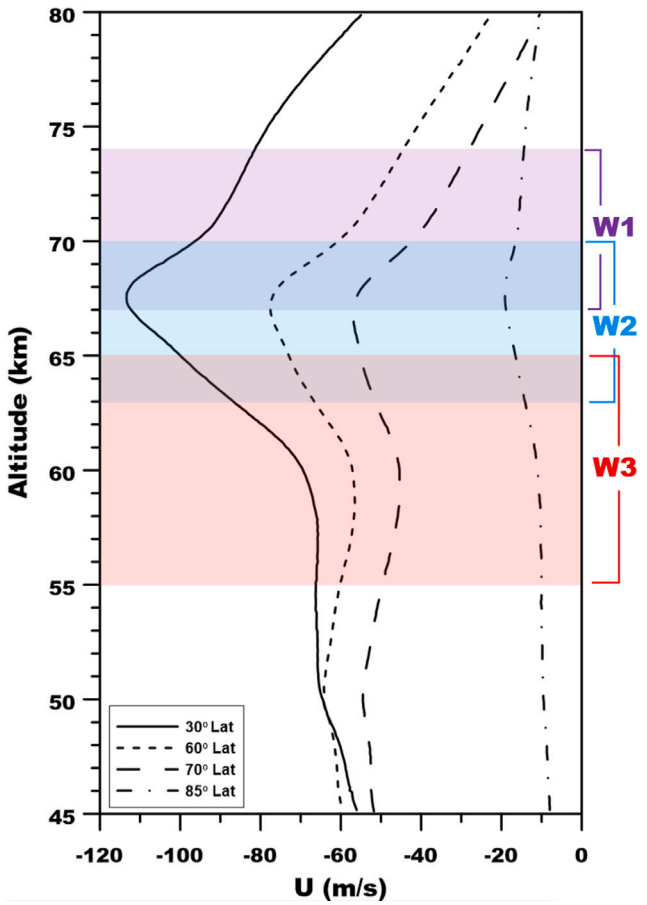

Fig. 10. Vertical profile of the zonal wind at different latitudes. These profiles were generated from Pioneer Venus probes in-situ measurements coupled with cloud tracking at several wavelengths, including the ones used in this work (Peralta et al., 2014).

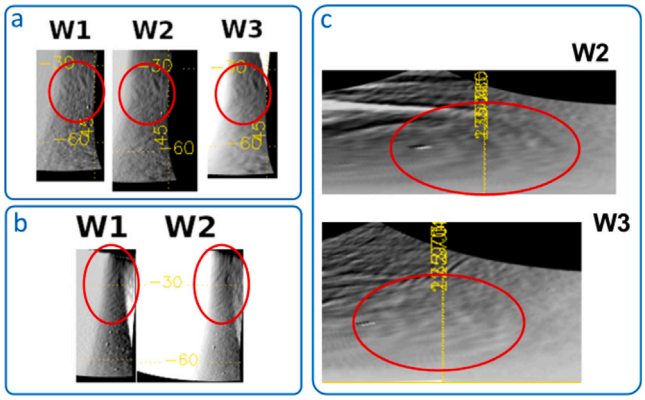

Fig. 11. Wave packets across several wavelength ranges. Case (a) was the only where the same wave packet was visible at the three wavelength ranges searched in this study. Case (b) was also the only one where the same wave packet was visible between W1 and W2 ranges. For case (c), we found more examples of wave packets on the top (W2) and middle clouds (W3). Wave packets are signalled with red circle frames.

wind shear brought by modelling (Lefèvre et al., 2018), differences in some packets are more pronounced although not exceeding 20% with one exception. Additionally, if we take the average values of vertical wavelength as presented in Table 3 and compare them with values that consider wind shear for the same altitude range, the difference amounts to less than 10% in the majority of wave packets. Given our current error estimations for these calculations, the limited precision of our measurements also exacerbates the similarities between both results of the calculation as seen in Table 5.

Table 5
Vertical Wavelengths calculated with wind shear (WS) contribution. We also include here the vertical wavelength calculated with the simpler form of the dispersion relation on Table 3.

VEx Orbit	Lat (°)	λ_z (km)	$\lambda_z(WS)$ (km)	$\delta_{\lambda_z(WS)}$ (km)
694 (W2)	−58.4	4	4	4
477 (W2)	−69.6	5	5	5
698 (W3)	−31.1	2	3	7
468 (W3)	−52.3	6	6	3
650 (W3)	−53.3	2	2	2
694 (W3)	−57.3	5	5	4
740 (W3)	−63.9	7	7	6
914 (W3)	−65.9	7	6	5
476 (W3)	−66.6	3	3	5
476 (W3)	−68.4	4	4	4
912 (W3)	−72.5	1	3	2
479 (W3)	−72.8	5	5	4
880 (W3)	−76.2	11	12	8
885 (W3)	−78.3	4	4	3

A possible reason for this might lay with the fact that most waves from which a value of λ_z could be calculated were located at latitudes polewards of −50°, where the vertical shear of the zonal wind ought to decrease, mitigating its effect on wave propagation.

5.2. Dayside vs. Nightside waves

The period of observation analysed in this work overlaps with the previous study of nightside lower cloud gravity waves described in Silva et al. (2021). The altitude range of the waves in this study (as explored in Section 5.1 and summarized in Table 4) is overall different than the region surveyed by infrared images on the nightside, which target the lower clouds at approximately 44–56 km depending on latitude (Silva et al., 2021; Titov et al., 2018). The general local time coverage is also distinct since for this study we are covering the dayside whereas Silva et al. (2021) covered the nightside.

As previously mentioned the number of images analysed in this data set is larger than the previous analogous studies however, the overall lower contrast coupled with the odd-even effect for shorter wavelengths results in a 40% decrease of images that were suitable for our analysis. The number of distinct packets observed on the dayside is less than half that on the nightside.

Fig. 12 shows the same distribution of distinct wave packets that were analysed in this work with the addition of previously observed nightside waves (Silva et al., 2021), and previous observations of waves on the dayside with VIRTIS (Peralta et al., 2008). The combination of the data sets provides a more even distribution of packets across longitude.

Fig. 13 shows that waves on the upper and lower cloud have overall similar spatial scales. However, the distribution of these properties appears to be slightly different between waves in both locations, particularly for the horizontal wavelength (Panel A) and the packet length (Panel C). The higher static stability on the upper clouds along with generally increased background zonal wind speed can play a role in this difference. Regarding the packet width, apart from the longer tail towards larger packets for dayside waves, the majority of waves share a closer distribution to their nightside counterpart, suggesting that both wave populations might share a dynamical origin. Additionally, the parameters associated with orientation (Panels D–F) are also similar, which is expected considering the formation and propagation of gravity waves over winds that flow in the same direction, between upper and lower cloud, although less so for the crest skew of dayside waves.

The similarity of the spatial scales of the morphological parameters of these waves may also be influenced by an observational bias towards the types of waves found in this study, given the spatial resolution

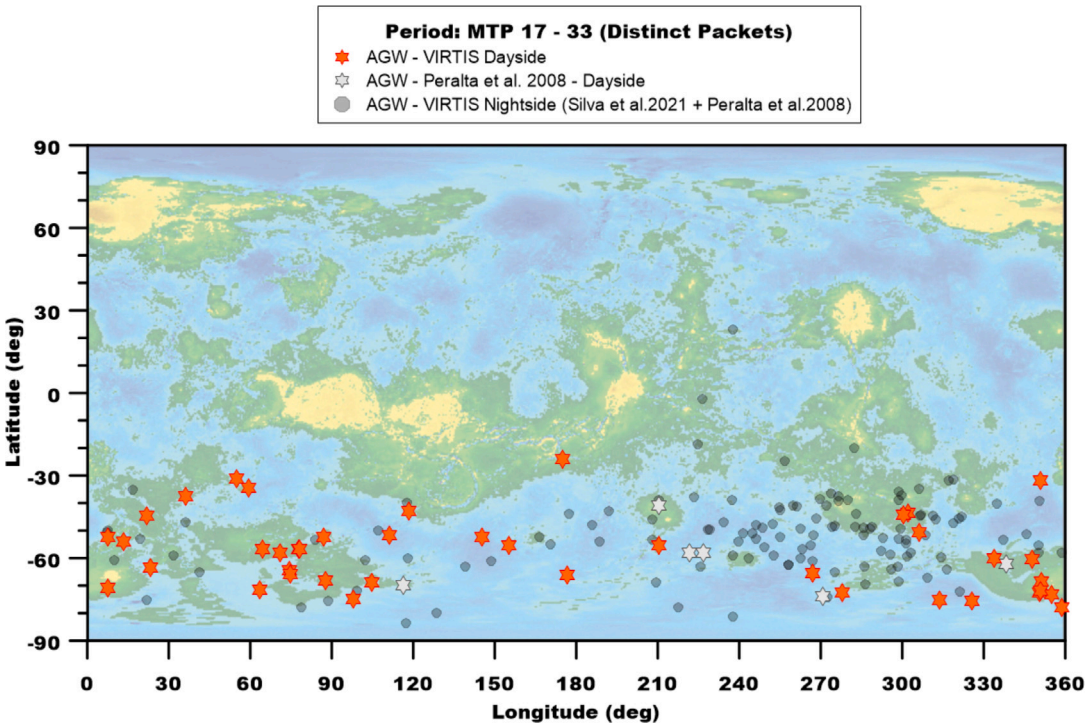

Fig. 12. Distribution of characterized gravity waves with VIRTIS data on the dayside upper cloud (red stars - this work; light grey - (Peralta et al., 2008)) and on the nightside lower cloud (shaded circles - (Silva et al., 2021)). Both data sets have identical observation periods. The period reference of 'MTP' refers to the codename of data volumes of the VIRTIS instrument. In this case between 17–33 corresponds to the before mentioned dates - August 2007 - October 2008. (For interpretation of the references to colour in this figure legend, the reader is referred to the web version of this article.)

of VIRTIS-M data. Nevertheless, should waves observed on the upper and lower cloud be forced by the same mechanism, convection would remain a likely source as concluded in Silva et al. (2021).

Regarding orientations, it could be expected that wave tilt and distortion in the form of crest skew increase for waves in the upper cloud, as both may rise with altitude and are tied with the wind shear environment (Orton et al., 2020). However, neither of these quantities is remarkably different between cloud levels. Such similarities are mirrored in the waves' properties dependence on latitude, although there appear to be slightly longer horizontal wavelengths and wider packets on the dayside (Fig. 14). The zonal wind speed on the upper and lower clouds is significantly different, with the former being between 30–40 m/s faster than in the lower cloud. However, most characterizations were made at visible wavelengths where the average zonal wind speed profile approaches what has also been measured in the lower cloud both in the Venus Express (Gorinov et al., 2021) era and more recent measurements with Akatsuki (Peralta et al., 2018). This can lead to further bias that can explain the similarities in most properties of these waves.

When comparing the intrinsic dynamics of waves in the upper and lower clouds (Fig. 15), it is evident that waves detected higher in the atmosphere seem to have overall greater speeds relative to their background zonal wind. This can be attributed to the increased static stability in the middle and upper clouds, where the identified wave packets propagate.

The observed lifetime of dayside waves (0.5 to 3 h) is shorter than on the nightside (0.5 to 6.5 h) although this is most likely caused by the more restricting observing conditions as described earlier.

Such changes would prompt visible differences in the vertical extent of gravity waves in the upper cloud however, from Fig. 16 it is clear that even their vertical extensions do not change dramatically with altitude, further reinforcing the assumption that waves on both cloud layers share the same forcing mechanism.

The statistical similarity in the properties of gravity waves observed in the dayside in the upper clouds reported here, and in the nightside in the lower clouds at 45–56 km reported in Silva et al. (2021) could be reconciled if gravity waves in both layers are excited by a common mechanism. Convection in the nearly neutrally stable atmospheric layer located around 50–55 km (Zasova et al., 2007; Tellmann et al., 2009; Ando et al., 2020) could produce simultaneous waves on both vertically stable atmospheric layers. Waves generated in the neutrally stable layer may propagate both downwards, where they are observed in infrared images on the nightside lower cloud, and upwards where they can be seen at visible and UV wavelengths on the dayside upper clouds (Lefèvre et al., 2018). This would produce waves that are not coupled to the underlying topography and in turn, are more sensitive to local time as is tentatively implied by both their distribution (Fig. 5) and properties (Fig. 7).

5.2.1. *Variations of the cloud convective layer*

Variations of the cloud convective layer with local time, such as those observed in temperature profiles with Akatsuki Radio Science instrument (Imamura et al., 2017), or inferred from model calculations (Imamura et al., 2014; Lefèvre et al., 2018) might provoke changes on gravity wave properties and excitation, should convection be the main source of these waves. The static stability profiles between morning and afternoon in Imamura et al. (2017) suggest that the convective layer changes considerably between both local time regions. A similar scenario is envisioned in Imamura et al. (2014) with stronger convection on the nightside. Radio occultation data from VEx does not show such variability however (Tellmann et al., 2009), and the model described in Lefèvre et al. (2018) which is arguably more comprehensive than in Imamura et al. (2014), do not report such changes. Regarding the data set presented here and in Silva et al. (2021), wave properties only seem to be influenced by local time on the dayside upper cloud, showing no appreciable change for the nightside data set.

5.2.2. *Further comparisons with previous work*

Another large survey of gravity waves in the upper clouds of Venus is presented in Piccialli et al. (2014), using images from VMC onboard

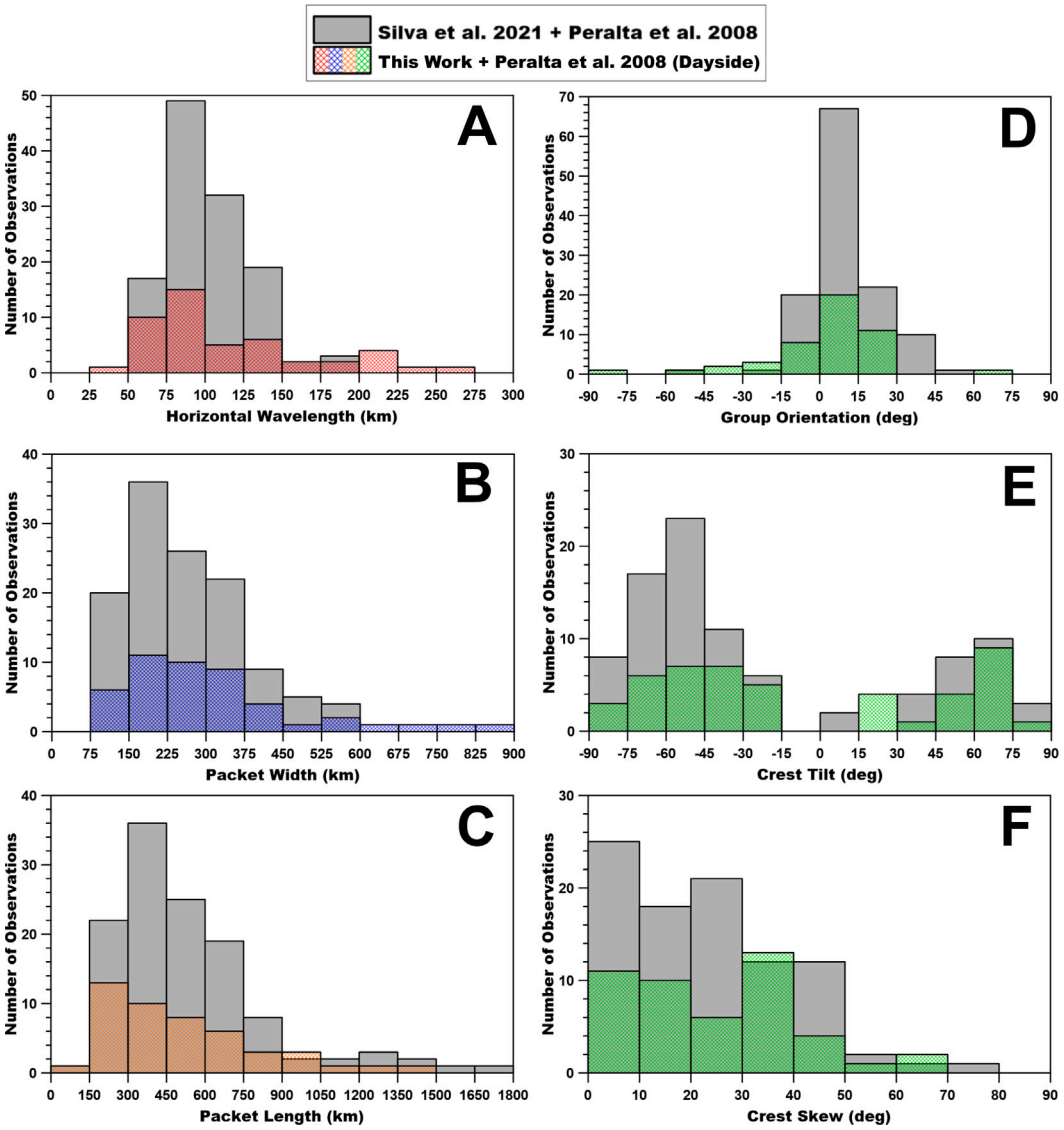

Fig. 13. Morphological properties of upper cloud dayside and lower cloud nightside atmospheric gravity waves observed with VIRTIS data. Organization of panels is identical to Fig. 6. Nightside and dayside data is taken from Peralta et al. (2008) and Silva et al. (2021).

VEx. The waves characterized in that analysis are confined to latitudes > 45°N and have reduced spatial dimensions of approximately one order of magnitude less when compared with the waves in the present work. We acknowledge that only images with spatial resolutions of approximately 1 km/pix were considered in Piccialli et al. (2014), which makes it more challenging to identify larger packets as those characterized here. Additionally, the small wave packets identified with VMC data are mostly oriented towards the pole, in contrast with the selection explored here. The difference in size may play a role in the orientation of the waves or how this orientation is influenced by the background wind environment. The predominance of the zonal wind at the wavelengths used in this work is still apparent at latitudes 60°–70° when compared to the meridional wind at the same altitude, which may affect the orientation of wave packets. Conversely, most of the waves visualized by VMC in Piccialli et al. (2014) were observed in the northern hemisphere, a region not covered with images by VIRTIS-M since the fast speed of VEx precluded observations with long exposure time. As such, additional differences may arise considering the wind field might not be symmetric relative to the equator at all times (Goncalves et al., 2019; Horinouchi et al., 2018).

Further evidence of wave activity was reported by Tellmann et al. (2012) as small-scale fluctuations on temperature profiles, using radio occultation data from VEx/VeRa. The wave parameters inferred based on the temperature fluctuations, which are interpreted as gravity waves, point to similar vertical wavelengths and intrinsic zonal phase speeds as reported in this work, but horizontal wavelengths are 3–4 times larger than the waves in this study. The authors also report an increased gravity wave activity at mid-to-high latitudes (60°–70°) providing a good correlation with the wave distribution shown in Fig. 5. The results of Tellmann et al. (2012) also suggest that gravity wave activity increases close to the subsolar point, but this was only confirmed for low latitude regions, which do not match the spatial distribution of waves reported in this work. Additional results with radio occultation data from the Akatsuki Radio Science experiment suggest the possibility of waves with smaller vertical scales than those explored in this study, with vertical wavelengths of less than 500 m (Imamura et al., 2018). Even though other wave characteristics are challenging to compare based on the results presented by the authors, the improved vertical resolution achieved in Imamura et al. (2018) shows promise, especially if coordinated with imaging data to have a complete three-dimensional characterization of a gravity wave.

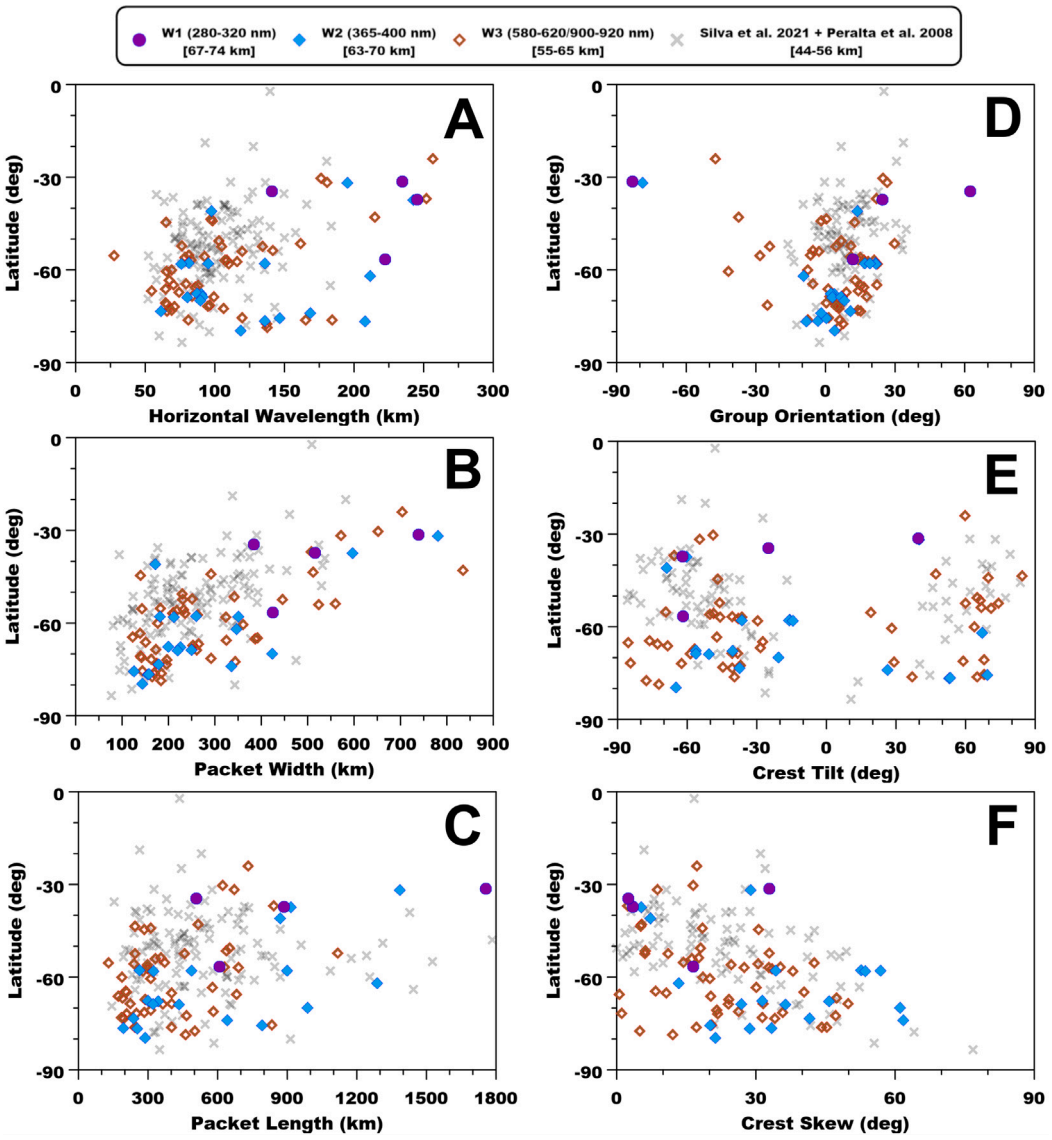

Fig. 14. Latitudinal dependence of morphological properties of dayside and nightside waves observed with VIRTIS data. Organization of panels is identical to Fig. 6. W2 data is coupled with dayside waves results from Peralta et al. (2008).

A similar comparison with results from modelling efforts on the vertical wavelength of convectively generated gravity waves can also be made considering the results in Imamura et al. (2014) and Lefèvre et al. (2018). However, the horizontal wavelengths achieved with these works (10–20 km) do not reproduce the larger horizontal wavelengths (∼ 100 km) observed here or in Peralta et al. (2008). Based on the images used for this study, it is difficult to confirm such small wave packets due to spatial resolution limitations, even though it is possible their occurrence may not be limited to high latitudes as presented in Piccialli et al. (2014). On another note, Lefèvre et al. (2018) points out that through the influence of wind shear, the wavefronts of packets reproduced by the model are more linear in shape, which is consistent with our observations. However, considering the apparently diminished influence of the vertical shear of the zonal wind on the vertical wavelength estimation (see Section 5.1.4), the shape of the packets observed in this study is possibly influenced by more parameters.

The presence of such a prominent mountainous region as *Ishtar Terra* could encourage the formation of gravity waves, which is one of the conclusions drawn by Piccialli et al. (2014) and also proposed by Tellmann et al. (2012), even though other sources like Kelvin–Helmholtz instabilities or convection are also mentioned. A topographic feature of that scale is not known to exist at similar latitudes in the southern hemisphere. Moreover, since the cloud top is expected to be lower at higher latitudes (Ignatiev et al., 2009), topographically generated waves might be able to travel more easily through regions of neutral or near-neutral stability by a type of 'wave tunnelling through a neutral barrier' effect first described in Sutherland and Yewchuk (2004) and also approached in modelling efforts by Lefèvre et al. (2020).

5.3. Comparison with stationary waves

Many stationary features found on Venus' atmosphere at the wavelength ranges used in this work are inferred to be a consequence or manifestation of gravity waves associated with topography (Fukuya et al., 2022; Kitahara et al., 2019; Peralta et al., 2017b).

On the dayside, these features have been observed by the Ultraviolet Imager (UVI) instrument onboard Akatsuki (Kitahara et al., 2019), which generates images centred at 283 and 365 nm, targeting similar altitude levels as W1 and W2 in this work. However, stationary waves are only clearly detected at 283 nm centred images. All features are found at locations associated with mountains and commonly have a single bow-shaped morphology, as opposed to the wave-trains

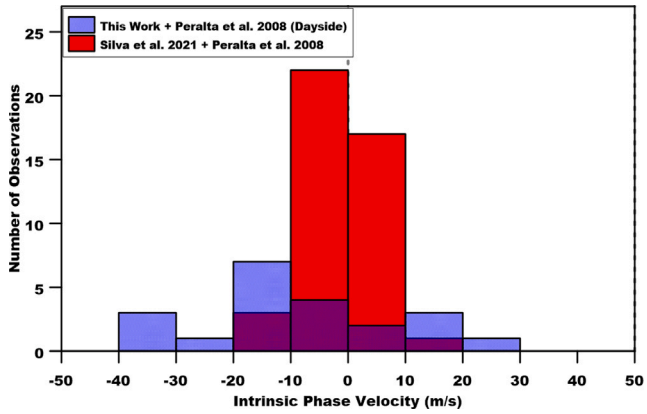

Fig. 15. Intrinsic phase velocity of gravity waves propagating on the upper and lower clouds from VIRTIS data within the same observing period. Nightside waves results are taken from Silva et al. (2021) and Peralta et al. (2008). We also include dayside waves data retrieved in Peralta et al. (2008). The average errors associated with dayside waves are approximately 9 m/s and for nightside waves around 6 m/s.

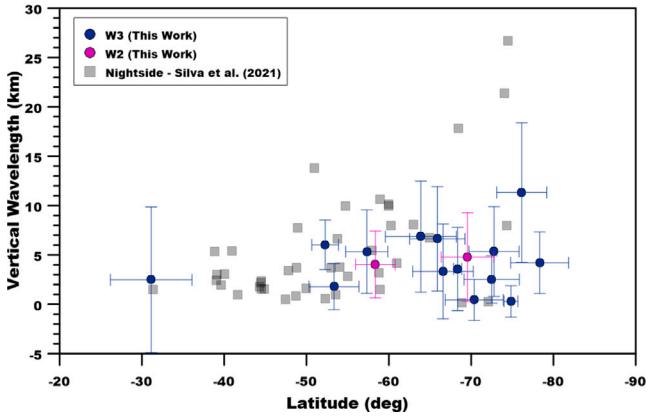

Fig. 16. Calculated vertical wavelengths from waves on the upper and lower cloud at their respective latitudes.

explored here. As reported in Kitahara et al. (2019), the features have a horizontal extension between 300–500 km and a north–south extension between 2000–3000 km. Considering that these features have a mostly perpendicular orientation to the zonal direction, we relate the before-mentioned values to packet length and packet width respectively.

The local distribution of packets found in this study and the stationary features observed by UVI never overlap, which is largely expected due to the equatorial orbit of the Akatsuki spacecraft as opposed to the previously mentioned polar orbit of Venus Express. The horizontal extensions of these stationary waves are overall smaller than the packet length of waves in this survey (see Table 1), although we must acknowledge the difference between the wave trains in this work (which feature a sequence of multiple crests-troughs) and those found by Kitahara et al. (2019) (usually single crest). Regarding meridional extension of the packets when compared to the packet width of the waves found by VIRTIS, there is a stark contrast in dimensions between the two populations of waves, with the crests of the bow-shaped features seen with UVI extending over 4 times the average width of VIRTIS waves. As already mentioned, the group orientation of the stationary waves observed is predominantly close to 0° however, taking the standard deviation of the group orientation from the mean (see Table 1), the alignment of the packets found in this study is less consistent (average variability of around 25° between packets at W2).

Similar comparisons can be established with stationary features found on brightness temperature images recorded by the Longwave Infrared Camera (LIR) onboard Akatsuki (Fukuya et al., 2022). These images show stationary wave trains, which greatly extend their zonal span, reaching values between 500–1500 km, revealing some consistency between wave populations there and in the present work. Note that the waves detected with LIR can be found on both dayside and nightside and the altitudes associated with these structures are centred at ~ 65 km (Taguchi et al., 2007).

Stationary and slow-moving features were also reported on the nightside atmosphere using VIRTIS-M at 3.8 and 5 μm, which shows its thermal emission of the upper cloud, on an extensive survey presented in Peralta et al. (2017b). The horizontal wavelengths of these structures are between 100–250 km, with packet lengths around 1000 km and widths extending within 1000–3000 km. Curiously the horizontal wavelengths found on travelling waves both on the day and nightsides (Peralta et al., 2008; Silva et al., 2021) are similar to what was measured for the stationary features seen on thermal emission. However, the packet lengths are on average double the size for stationary features than for travelling waves at the same altitude region on the dayside, even though there might reside here an observational bias, as the sample from Peralta et al. (2017b) was much more numerous. Regardless, we observe the same tendency on the packet widths, extending far beyond what is observed for travelling waves.

Given the unexpected discovery of the large bow-shaped stationary wave reported in Fukuhara et al. (2017) and the later additional detections of more stationary features on the atmosphere of Venus, modelling efforts were readily directed to reproduce these observations. One such effort (Lefèvre et al., 2020) was able to convincingly replicate the characteristics of the stationary waves detected by the Japanese space mission, with wave features that possess horizontal wavelengths with comparable values to those observed in this study. However, other morphological aspects and vertical wavelengths are remarkably different, the latter which exceeds more than 5 times the average observed here, along with the fact that these calculations model stationary features, unlike our detections.

Although differential coverage challenges interpretations over the distribution of packets between UVI and VIRTIS-M on the dayside reflected clouds, both wave populations seem disconnected in terms of their generating mechanisms, further emphasized by their different properties with particular attention to the packet width. For the waves found on the nightside thermal emission, we can find a better agreement between both populations and their distributions partially overlap. However, the large difference between the sample size of both data sets and the same contrast regarding packet widths reinforce the argument that the waves found in this study are not generated by flow over topography.

6. Conclusions

We have explored atmospheric waves on the dayside upper cloud of Venus by observing four narrow wavelength bands to characterize wave activity across different altitudes within the upper cloud. This survey took data from an analogous period on which nightside lower cloud waves were characterized (Silva et al., 2021) to investigate how wave properties change with altitude within the cloud deck of Venus and if there is any communication of mesoscale wave activity between lower and upper clouds.

This search was partially compromised by data quality issues brought by the small contrast of VIRTIS images, which made it challenging to evaluate wave activity, especially at W1 wavelengths (280–320 nm). Although this fact made it difficult to verify the three-dimensional structure of wave packets by observing across the three wavelength ranges chosen, a substantial number of waves was still characterized, especially at the visible range where fewer atmospheric features have been described in the past.

Dayside upper cloud wave packets share similar orientations and many properties with their siblings on the lower cloud, both in terms

of their spatial sizes and intrinsic dynamics and trajectories, although waves on the upper cloud seem to have a different distribution of wavelengths and tend to move faster relative to the background wind than waves in the lower layer. It is also noticeable that some morphological properties of waves are enhanced close to the evening terminator where wave activity is slightly increased as well. Continuous analysis of the extended VIRTIS data set (until the end of the mission in 2014) would yield more concluding results in this matter.

Waves on the lower and upper clouds, at 44–56 and 60–74 km respectively and observed on the nightside and dayside on different images, have similar mean properties in terms of their wavelengths and orientations. This suggests a similar origin even if both layers are separated by a neutrally stable layer at approximately 50–55 km. Convection in the intermediate neutrally stable layer could be the source of gravity waves in both layers.

From comparisons with waves associated with topographical features, we additionally make the tentative conclusion that the waves found in this study are probably not forced by topography. However, we encourage further exploration of the VIRTIS-M dayside data to bridge the gap between past and present missions to Venus and also expand the search for waves to its fullest.

Acronyms

VIRTIS-M: Visible and Infrared Thermal Imaging Spectrometer-Mapper; VMC: Venus Monitoring Camera; VEx: Venus Express; ESA: European Space Agency; IR2: 2 μm Camera; UV: Ultraviolet; IR: Infrared; W1: 280–320 nm; W2: 365–400 nm; W3: 580–620/900–920 nm; PLIA: Planetary Laboratory for Image Analysis; PL: Packet Length; PW: Packet Width; LT: Local Time; Lat: Latitude; UVI: Ultraviolet Imager; LIR: Longwave Infrared Camera; VeRa: Venus Radio Science;

CRediT authorship contribution statement

José E. Silva: Writing – review & editing, Writing – original draft, Visualization, Validation, Software, Resources, Methodology, Investigation, Formal analysis, Data curation, Conceptualization. **Javier Peralta:** Writing – review & editing, Validation, Software, Investigation, Formal analysis. **Alejandro Cardesín-Moinelo:** Writing – review & editing, Validation, Data curation. **Ricardo Hueso:** Writing – review & editing, Visualization, Validation, Software. **Daniela Espadinha:** Writing – review & editing, Visualization. **Yeon Joo Lee:** Writing – review & editing, Validation, Supervision, Resources, Project administration, Funding acquisition.

Declaration of competing interest

The authors declare that they have no known competing financial interests or personal relationships that could have appeared to influence the work reported in this paper.

Data availability

Data will be made available on request.

Acknowledgements

This work was supported by the Institute for Basic Science, South Korea (IBS- R035-C1). We also acknowledge the support of the European Space Agency and the associated funding bodies Centre National d'Etudes Spatiales (France) and Agenzia Spaziale Italiana (Italy) as well as the full team behind the VIRTIS instrument, Venus Express space mission and the PSA archives (ESAPlanetaryScienceArchive). R.Hueso was supported by Grant PID2019-109467GB-I00 funded by MCIN/AEI/10.13039/501100011033, Spain/ and by Grupos Gobierno Vasco, Spain IT1742-22. J. Peralta thanks EMERGIA funding from Junta de Andalucia in Spain (code: EMERGIA20_00414). J.S. acknowledges that J.P. and R.H. contributed greatly with the software used to carry out this work and A.C. for help with interpreting the VIRTIS data set. J.S. also acknowledges the leadership and supervision of Y.J.L. Finally, J.S. acknowledges that all co-authors contributed in the review of this work before its submission.

References

Alexander, M., et al., 2010. Recent developments in gravity-wave effects in climate models and the global distribution of gravity-wave momentum flux from observations and models. Q. J. R. Meteo. Soc. 136, 1103–1124. http://dx.doi.org/10.1002/qj.637.

Ando, H., et al., 2020. Thermal structure of the Venusian atmosphere from the sub-cloud region to the mesosphere as observed by radio occultation. Sci. Rep. 10, 3448. http://dx.doi.org/10.1038/s41598-020-59278-8.

Cardesin-Moinelo, A., et al., 2010. Calibration of hyperspectral imaging data: VIRTIS-M onboard Venus express. IEEE Trans. Geosci. Remote Sens. 48, 3941–3950. http://dx.doi.org/10.1109/TGRS.2010.2064325.

Cottini, V., et al., 2015. Water vapor near Venus cloud tops from VIRTIS-H/Venus express observations 2006–2011. Planet. Space Sci. 113, 219–225. http://dx.doi.org/10.1016/j.pss.2015.03.012.

Drossart, P., et al., 2007. Scientific goals for the observation of Venus by VIRTIS on ESA/Venus express mission. Planet. Space Sci. 55, 1653–1672. http://dx.doi.org/10.1016/j.pss.2007.01.003.

Fukuhara, T., et al., 2017. Large stationary gravity wave in the atmosphere of Venus. Nat. - Geosci. 10, 85–88. http://dx.doi.org/10.1038/NGEO2873.

Fukuya, K., et al., 2022. Horizontal structures of bow-shaped mountain wave trains seen in thermal infrared images of Venusian clouds taken by Akatsuki LIR. Icarus 378, 114936. http://dx.doi.org/10.1016/j.icarus.2022.114936.

Garcia, R., et al., 2009. Gravity waves in the upper atmosphere of Venus revealed by CO2 nonlocal thermodynamic equilibrium emissions. J. Geophys. Res. 114, E00B32. http://dx.doi.org/10.1029/2008JE003073.

Gilli, G., et al., 2020. Impact of gravity waves on the middle atmosphere of Mars: A non-orographic gravity wave parameterization based on global climate modeling and MCS observations. J. Geophys. Res. - Planets e05873. http://dx.doi.org/10.1029/2018JE005873.

Gilli, G., et al., 2021. Venus upper atmosphere revealed by a GCM: II. Model validation with temperature and density measurements. Icarus 24. http://dx.doi.org/10.1016/j.icarus.2021.114432.

Goncalves, R., et al., 2019. Venus' cloud top wind study: Coordinated Akatsuki/UVI with cloud tracking and TNG/HARPS-N with Doppler velocimetry observations. Icarus 335, 113418. http://dx.doi.org/10.1016/j.icarus.2019.113418.

Gorinov, D., et al., 2021. Winds in the lower cloud level on the nightside of Venus from VIRTIS-M (Venus-Express) 1.74 μm images. Atmosphere 12 (186), http://dx.doi.org/10.3390/atmos12020186.

Holton, J., 2004. An Introduction to Dynamic Meteorology, fourth ed. Elsevier Inc., ISBN: 0-12-354015-1, Chapter 7.

Horinouchi, T., et al., 2018. Mean winds at the cloud top of Venus obtained from two-wavelength UV imaging by Akatsuki. Earth Planets Space 70, 19. http://dx.doi.org/10.1186/s40623-017-0775-3.

Horinouchi, T., et al., 2020. How waves and turbulence maintain the super-rotation of Venus' atmosphere. Sci 368, 405–409. http://dx.doi.org/10.1126/science.aaz4439.

Hou, A., Farrel, B., 1987. Superrotation induced by critical-level absorption of gravity waves on Venus: An assessment. J. Atmos. Sci. 44, 1049–1061. http://dx.doi.org/10.1175/1520-0469(1987)044<1049:SIBCLA>2.0.CO;2.

Hueso, R., et al., 2010. The Planetary Laboratory for Image Analysis (PLIA). Adv. Space Res. 46, 1120–1138. http://dx.doi.org/10.1016/j.asr.2010.05.016.

Hueso, R., et al., 2012. Assessing the long-term variability of Venus winds at cloud level from VIRTIS–Venus express. Icarus 217, 585–598. http://dx.doi.org/10.1016/j.icarus.2011.04.020.

Hueso, R., et al., 2015. Six years of Venus winds at the upper cloud level from UV, visible and near infrared observations from VIRTIS on Venus express. Planet. Space Sci. 113–114, 78–99. http://dx.doi.org/10.1016/j.pss.2014.12.010.

Iga, S., Matsuda, Y., 2005. Shear instability in a shallow water model with implications for the Venus atmosphere. J. Atmos. Sci. 62, 2514–2527. http://dx.doi.org/10.1175/JAS3484.1.

Ignatiev, N., et al., 2009. Altimetry of the Venus cloud tops from the Venus express observations. J. Geophys. Res. 114, E00B43. http://dx.doi.org/10.1029/2008JE003320.

Imamura, T., et al., 2014. Inverse insolation dependence of Venus' cloud-level convection. Icarus 228, 181–188. http://dx.doi.org/10.1016/j.icarus.2013.10.012.

Imamura, T., et al., 2017. Initial performance of the radio occultation experiment in the Venus orbiter mission Akatsuki. Earth Planets Spacce 69, 137. http://dx.doi.org/10.1186/s40623-017-0722-3.

Imamura, T., et al., 2018. Fine vertical structures at the cloud heights of Venus revealed by radio holographic analysis of Venus express and Akatsuki radio occultation data. J. Geophys. Res.: Planets 123, 2151–2161. http://dx.doi.org/10.1029/2018JE005627.

Jessup, K., et al., 2015. Coordinated hubble space telescope and Venus express observations of Venus' upper cloud deck. Icarus 258, 309–336. http://dx.doi.org/10.1016/j.icarus.2015.05.027.

Kitahara, T., et al., 2019. Stationary features at the cloud top of Venus observed by ultraviolet imager onboard Akatsuki. J. Geophys. Res.: Planets 124, 1266–1281. http://dx.doi.org/10.1029/2018JE005842.

Kouyama, T., et al., 2017. Topographical and local time dependence of large stationary gravity waves observed at the cloud top of Venus. Geophys. Res. Lett. 44, 12,098–12,105. http://dx.doi.org/10.1002/2017GL075792.

Lee, Y., et al., 2022. Reflectivity of Venus's dayside disk during the 2020 observation campaign: Outcomes and future perspectives. Planet. Sci. J. 3, 209.

Lefèvre, M., et al., 2018. Three-dimensional turbulence-resolving modeling of the Venusian cloud layer and induced gravity waves: Inclusion of conplete radiative transfer and wind shear. J. Geophys. Res.: Planets 123, 2773–2789. http://dx.doi.org/10.1029/2018JE005679.

Lefèvre, M., et al., 2020. Mesoscale modeling of Venus' bow-shape waves. Icarus 335, 113376. http://dx.doi.org/10.1016/j.icarus.2019.07.010.

Machado, P., et al., 2017. Venus cloud-tracked and doppler velocimetry winds from CFHT/ESPaDOnS and Venus express/VIRTIS in April 2014. Icarus 285, 8–26. http://dx.doi.org/10.1016/j.icarus.2016.12.017.

Machado, P., et al., 2021. Venus atmospheric dynamics at two altitudes: Akatsuki and Venus express cloud tracking, ground-based Doppler observations and comparison with modelling. Atmosphere 12, 506. http://dx.doi.org/10.3390/atmos12040506.

Marcq, E., et al., 2013. Variations of sulphur dioxide at the cloud top of Venus's dynamic atmosphere. Nature-Geosci. 6, 25–28. http://dx.doi.org/10.1038/ngeo1650.

Marcq, E., et al., 2020. Climatology of SO2 and UV absorber at Venus' cloud top from SPICAV-UV nadir dataset. Icarus 335, 113368. http://dx.doi.org/10.1016/j.icarus.2019.07.002.

Nappo, C., 2002. Introduction to Atmospheric Gravity Waves. In: International Geophysics Series, vol. 85, Chapter 1 and 2.

Orton, G., et al., 2020. A survey of small-scale waves and wave-like phenomena in Jupiter's atmosphere detected by JunoCam. J. Geophys. Res.: Planets 125, http://dx.doi.org/10.1029/2019JE006369, e2019JE006369.

Peralta, J., et al., 2007. A reanalysis of Venus winds at two cloud levels from Galileo SSI images. Icarus 190, 467–477. http://dx.doi.org/10.1016/j.icarus.2007.03.028.

Peralta, J., et al., 2008. Characterization of mesoscale gravity waves in the upper and lower clouds of Venus from VEX-VIRTIS images. J. Geophys. Res. 113, E00B18. http://dx.doi.org/10.1029/2008JE003185.

Peralta, J., et al., 2014. Analytical solution for waves in planets with atmospheric superrotation. I. Acoustic and inertia-gravity waves. Astrophys. J. Suppl. Ser. 213:17, 18. http://dx.doi.org/10.1088/0067-0049/213/1/17.

Peralta, J., et al., 2017a. Overview of useful spectral regions for Venus: An update to encourage observations complementary to the Akatsuki mission. Icarus 288, 235–239. http://dx.doi.org/10.1016/j.icarus.2017.01.027.

Peralta, J., et al., 2017b. Stationary waves and slowly moving features in the night upper clouds of Venus. Nat. - Astron. 187. http://dx.doi.org/10.1038/s41550-017-0187.

Peralta, J., et al., 2018. Nightside winds at the lower clouds of Venus with Akatsuki/IR2: Longitudinal, local time and decadal variations from comparison with previous measurements. Astrophys. J. Suppl. Ser. 239 (29), 15pp. http://dx.doi.org/10.3847/1538-4365/aae844.

Peralta, J., et al., 2019. Morphology and dynamics of Venus's middle clouds with Akatsuki/IR1. Geophys. Res. Lett. 46, 2399–2407. http://dx.doi.org/10.1029/2018GL081670.

Perez-Hoyos, S., et al., 2018. Venus upper clouds and the UV absorber from MESSENGER/MASCS observations. J. Geophys. Res.: Planets 123, 145–162. http://dx.doi.org/10.1002/2017JE005406.

Piccialli, A., et al., 2014. High latitude gravity waves at the Venus cloud tops as observed by the Venus monitoring camera on board Venus express. Icarus 227, 94–111. http://dx.doi.org/10.1016/j.icarus.2013.09.012.

Piccioni, G., et al., 2007. VIRTIS: The Visible and Infrared Thermal Imaging Spectrometer, vol. SP 1295, ESA Special Publication, p. 27.

Sanchez-Lavega, A., 2011. Introduction to Planetary Atmospheres. CRC Press, Taylor and Francis group, Chapter 8.

Sanchez-Lavega, A., et al., 2008. Variable winds on Venus mapped in three dimensions. Geophys. Res. Lett. 35, L13204. http://dx.doi.org/10.1029/2008GL033817.

Sanchez-Lavega, A., et al., 2017. The atmospheric dynamics of Venus. Space Sci. Rev. 212, 1541–1616. http://dx.doi.org/10.1007/s11214-017-0389-x.

Schubert, G., Walterscheild, R., 1984. Propagation of small-scale acoustic-gravity waves in the Venus atmosphere. J. Atmos. Sci. 41 (7), 1201–1213. http://dx.doi.org/10.1175/1520-0469(1984)041<1202:POSSAG>2.0.CO;2.

Seiff, A., 1982. Dynamical implications of the observed thermal contrasts in Venus' upper atmosphere. Icarus 51 (3), 574–592. http://dx.doi.org/10.1016/0019-1035(82)90147-6.

Silva, J., et al., 2021. Characterising atmospheric gravity waves on the nightside lower clouds of Venus: A systematic study. Astron. Astrophys. 649 (A34), 15. http://dx.doi.org/10.1051/0004-6361/202040193.

Sutherland, B.R., 2010. Internal Gravity Waves. Cambridge University Press, Chapter 1.

Sutherland, B., Yewchuk, K., 2004. Internal wave tunnelling. J. Fluid Mech. 511, 125–134. http://dx.doi.org/10.1017/S0022112004009863.

Svedhem, H., et al., 2007. Venus express—The first European mission to Venus. Planet. Space Sci. 55, 1636–1652. http://dx.doi.org/10.1016/j.pss.2007.01.013.

Taguchi, M., et al., 2007. Longwave infrared camera onboard the Venus climate orbiter. Adv. Space Res. 40 (6), 861–868. http://dx.doi.org/10.1016/j.asr.2007.05.085.

Takagi, M., et al., 2018. Three-dimensional structures of thermal tides simulated by a Venus GCM. J. Geophys. Res.: Planets 123, 335–352. http://dx.doi.org/10.1002/2017JE005449.

Tellmann, S., et al., 2009. Structure of the Venus neutral atmosphere as observed by the radio science experiment VeRa on Venus express. J. Geophys. Res. 114 (9), E00B36. http://dx.doi.org/10.1029/2008JE003204.

Tellmann, S., et al., 2012. Small-scale temperature fluctuations seen by the VeRa radio science experiment on Venus express. Icarus 221, 471–480. http://dx.doi.org/10.1016/j.icarus.2012.08.023.

Titov, D., et al., 2006. Venus express science planning. Planet. Space Sci. 54, 1279–1297. http://dx.doi.org/10.1016/j.pss.2006.04.017.

Titov, D., et al., 2018. Clouds and Hazes of Venus. Space Sci. Rev. 214 (126), 61. http://dx.doi.org/10.1007/s11214-018-0552-z.

Zasova, L., et al., 2007. Structure of the Venus atmosphere. Planet. Space Sci. 55, 1712–1728. http://dx.doi.org/10.1016/j.pss.2007.01.011.